JOURNAL OF GEOPHYSICAL RESEARCH, VOL. 112, D02304, doi:10.1029/2006JD007268, 2007

Satellite chartography of atmospheric methane from SCIAMACHY on board ENVISAT: 2. Evaluation based on inverse model simulations

P. Bergamaschi,[1] C. Frankenberg,[2] J. F. Meirink,[3,4] M. Krol,[1,5,6] F. Dentener,[1] T. Wagner,[2] U. Platt,[2] J. O. Kaplan,[1] S. Körner,[7] M. Heimann,[7] E. J. Dlugokencky,[8] and A. Goede[3]

Received 7 March 2006; revised 24 May 2006; accepted 18 August 2006; published 24 January 2007.

[1] We extend the analysis of a global CH_4 data set retrieved from SCIAMACHY (Frankenberg et al., 2006) by making a detailed comparison with inverse TM5 model simulations for 2003 that are optimized versus high accuracy CH_4 surface measurements from the NOAA ESRL network. The comparison of column averaged mixing ratios over remote continental and oceanic regions shows that major features of the atmospheric CH_4 distribution are consistent between SCIAMACHY observations and model simulations. However, the analysis suggests that SCIAMACHY CH_4 retrievals may have some bias that depends on latitude and season (up to ~30 ppb). Large enhancements of column averaged CH_4 mixing ratios (~50–100 ppb) are observed and modeled over India, Southeast Asia, and the tropical regions of South America, and Africa. We present a detailed comparison of observed spatial patterns and their seasonal evolution with TM5 $1° \times 1°$ zoom simulations over these regions. Application of a new wetland inventory leads to a significant improvement in the agreement between SCIAMACHY retrievals and model simulations over the Amazon basin during the first half of the year. Furthermore, we present an initial coupled inversion that simultaneously uses the surface and satellite observations and that allows the inverse system to compensate for the potential systematic bias. The results suggest significantly greater tropical emissions compared to either the a priori estimates or the inversion based on the surface measurements only. Emissions from rice paddies in India and Southeast Asia are relatively well constrained by the SCIAMACHY data and are slightly reduced by the inversion.

Citation: Bergamaschi, P., et al. (2007), Satellite chartography of atmospheric methane from SCIAMACHY on board ENVISAT: 2. Evaluation based on inverse model simulations, *J. Geophys. Res.*, *112*, D02304, doi:10.1029/2006JD007268.

1. Introduction

[2] Atmospheric CH_4 is the second-most important anthropogenic greenhouse gas (GHG) after CO_2. Including chemically induced indirect effects, the radiative forcing of CH_4 is estimated at ~0.6 Wm^{-2} [*IPCC*, 2001; *Lelieveld et al.*, 1998]. Compared to preindustrial levels (year 1800) atmospheric CH_4 has increased by a factor of 2.5 [*Etheridge et al.*, 1992]. From ice core measurements it is known that present atmospheric levels of methane are unprecedented during at least the last 650,000 years [*Petit et al.*, 1999; *Spahni et al.*, 2005]. During the last few years atmospheric CH_4 has almost stabilised [*Dlugokencky et al.*, 2003], but there is a high risk that CH_4 may further increase in the future [*Dentener et al.*, 2005; *IPCC*, 2001], due to both anthropogenic activities and potential feedbacks by climate change [*Shindell et al.*, 2004]. Hence, there is a need to better quantify CH_4 emissions, including their regional and temporal distribution, and attribution to the different CH_4 sources. Furthermore, CH_4 is included in the United Nations Framework Convention on Climate Change (UNFCCC) and the Kyoto protocol, which require reporting and verification of national total anthropogenic emissions [*Bergamaschi et al.*, 2004; *IPCC*, 2000].

[3] Observed emission rates from many CH_4 sources vary by orders of magnitude over small spatial and temporal scales, so extrapolation of these emissions to global and annual scales results in large uncertainties for bottom-up inventories. Therefore, complementary top-down approaches using atmospheric observations and inverse modeling are indispensable. Such studies have been performed for the major GHGs CO_2 [*Gurney et al.*, 2002;

[1]European Commission - DG Joint Research Centre, Institute for Environment and Sustainability, Ispra, Italy.
[2]Institute of Environmental Physics, University of Heidelberg, Heidelberg, Germany.
[3]Royal Netherlands Meteorological Institute, De Bilt, Netherlands.
[4]Institute for Marine and Atmospheric Research Utrecht, University of Utrecht, Utrecht, Netherlands.
[5]Wageningen University and Research Centre, Wageningen, Netherlands.
[6]Netherlands Institute for Space Research, Utrecht, Netherlands.
[7]Max Planck Institute for Biogeochemistry, Jena, Germany.
[8]Global Monitoring Division, Earth System Research Laboratory, NOAA, Boulder, Colorado, USA.

0148-0227/07/2006JD007268$09.00

Rödenbeck et al., 2003], CH_4 [*Bergamaschi et al.*, 2000, 2005; *Chen and Prinn*, 2006; *Hein et al.*, 1997; *Houweling et al.*, 1999; *Mikaloff Fletcher et al.*, 2004a, 2004b] and N_2O [*Hirsch et al.*, 2006; *Prinn et al.*, 1990], mainly based on ground-based discrete sampling and in situ measurements. Despite extension of the ground-based measurements during the past two decades, many very important source regions are still poorly sampled by existing monitoring sites. Only recently, CH_4 measurements from satellites became available, namely from the SCIAMACHY instrument on ENVISAT which is in orbit since March 2002 [*Buchwitz et al.*, 2005a, 2005b; *Frankenberg et al.*, 2006, 2005a]. In contrast to midinfrared measurements by IMG (which was in operation only from August 1996 to June 1997) [*Clerbaux et al.*, 2003] and by follow-on instruments (AIRS [*Crevoisier et al.*, 2003], IASI [*Turquety et al.*, 2004]), SCIAMACHY CH_4 measurements are based on near-infrared solar absorption spectra and hence also sensitive towards the boundary layer and lower troposphere. Therefore, SCIAMACHY is very well suited for detection of signals directly related to emissions at the surface. However, very high precision and relative accuracy of the column averaged mixing ratios (<1–2%) is required to apply these measurements to inverse modeling [*Meirink et al.*, 2006]. We use the term "relative accuracy" to describe the internal consistency of a data set in space and time (i.e., covering systematic errors which may vary in space and time) and "absolute accuracy" as measure for the potential deviation of the measurements from the true values (i.e., covering also systematic errors which are constant in space and time). For application in inverse modeling, in particular the relative accuracy is important, since already small spatial or temporal biases of observations lead to systematic errors of derived emission distributions [*Meirink et al.*, 2006], while any small constant systematic error has only a small impact on derived global total emissions, but not on their spatio-temporal distribution. Such constant systematic errors, however, become important, if different data sets are compared.

[4] *Frankenberg et al.* [2006, 2005a] presented CH_4 retrievals for 2003–2004, demonstrating that the north-south gradient as well as regions with enhanced methane levels can be clearly identified from space. Comparison with forward simulations based on the TM4 model showed also some discrepancies, particularly in the tropics, where SCIAMACHY retrievals yield higher CH_4 total column average mixing ratios than model simulations. In this paper we extend the analysis of *Frankenberg et al.* [2006] by using inverse model simulations to quantitatively evaluate potential errors in both retrievals and model simulations. The specific goals of this extended analysis are threefold:

1.1. Evaluation of SCIAMACHY Retrievals Over Remote Areas

[5] Only limited information is available from direct validation of SCIAMACHY data by other measurements such as ground-based Fourier Transform Spectrometer (FTS) measurements from the NDSC network [*Dils et al.*, 2006]. Particular difficulties of the direct comparison of these measurements are (1) that they may probe different air masses (this is especially the case when comparing SCIAMACHY data with FTS sites on mountains), (2) the limited number of co-located cloud-free measurements, (3) the sparse distribution of FTS sites over the globe, and (4) the limited precision and accuracy of the FTS measurements. *Dils et al.* [2006] estimated the precision of these FTS measurements at 3% and the relative accuracy at 7%, which is significantly below the precision and (relative) accuracy targets of <1–2% of the SCIAMACHY measurements [*Meirink et al.*, 2006]. In contrast, discrete-sample and in situ measurements of CH_4 by NOAA from a comprehensive global air sampling network have very high precision and absolute accuracy (~0.1 %) [*Dlugokencky et al.*, 2005]. These measurements, however, are probing the Earth surface, and information about the vertical distribution of CH_4 is required to render these measurements amenable for comparison with column averaged SCIAMACHY measurements. In this paper we use inverse model simulations to create 3D model fields with an optimal degree of consistency with these high-accuracy surface observations. Over remote regions these model fields constitute a good reference for comparison with SCIAMACHY retrievals, and are relatively insensitive to a range of different inversion scenarios.

1.2. Comparison of Small-Scale Patterns Over CH_4 Source Regions

[6] Over source regions with strong emissions, model simulations strongly depend on the applied a priori bottom-up inventories. Thus, even after optimisation with the surface measurements, the a posteriori simulations may have considerable uncertainties and errors in small scale spatial patterns. As SCIAMACHY provides almost global coverage (apart from data selection related, e.g., to clouds), it offers the opportunity to analyse observed and simulated spatial patterns arising from strong surface sources in detail. For this purpose we apply a multizoom version of the TM5 model [*Krol et al.*, 2005], which allows us to zoom in over the major continental source regions, including the tropics.

1.3. Initial Combined Inversion Using Both Surface Observations and SCIAMACHY Data

[7] In a first attempt to investigate potential implications of the SCIAMACHY measurements on the distribution of global CH_4 sources, we perform a combined inversion using both surface observations and SCIAMACHY data. This exercise also aims to evaluate the degree of consistency between surface and satellite observations. In this paper we restrict our analysis to year 2003.

2. Measurements

2.1. SCIAMACHY Measurements

[8] We use the SCIAMACHY retrievals, version V1.1, as described by *Frankenberg et al.* [2006, 2005a, 2005b]. This product represents the measured total column of CH_4, denoted $V_{meas}(CH_4)$, normalized to the measured total column of CO_2, $V_{meas}(CO_2)$. $V_{meas}(CH_4)$ and $V_{meas}(CO_2)$ are derived from neighbouring spectral regions in SCIAMACHY channel 6, ensuring very similar light path distributions for both species (fitting window: CH_4: 1631–1670 nm; CO_2: 1563–1585 nm). The column averaged CH_4 mixing ratio, $\overline{VMR}(CH_4)$, is obtained by

$$\overline{VMR}(CH_4) = \frac{V_{meas}(CH_4)}{V_{meas}(CO_2)} \cdot \overline{VMR}_{TM3}(CO_2) \qquad (1)$$

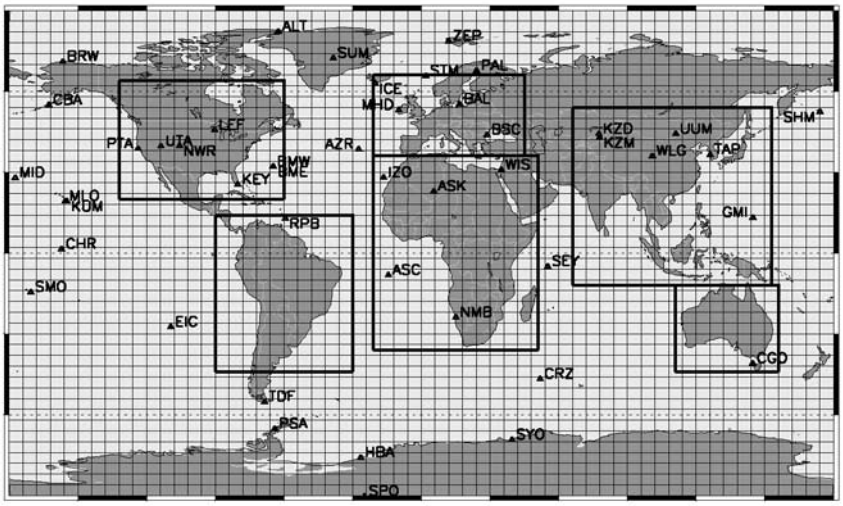

Figure 1. Surface air sampling sites from the NOAA network (see also Table 1). The six rectangles show the boundaries of the zoom regions over North America, South America, Europe, Africa, Asia, and Australia, which are run at $1^\circ \times 1^\circ$ resolution (see section 3.1). The global grid illustrates the $6^\circ \times 4^\circ$ resolution used for the base functions, which however, is then refined to $3^\circ \times 2^\circ$ in the final global simulation.

using modeled column averaged mixing ratios of CO_2 ($\overline{VMR}_{TM3}(CO_2)$). CO_2 simulations were performed using the TM3-MPI 3.8 model [*Heimann and Koerner*, 2003] and are similar to those described in *Frankenberg et al.* [2006]. However, the new, updated simulations applied in this paper use CO_2 biomass burning from the Global Fire Emissions Database (GFED) version 1 [*van der Werf et al.*, 2004] instead of EDGAR 3.2 [*Olivier and Berdowski*, 2001]. They are forward CO_2 simulations with corrections for a global offset and atmospheric increase optimized to agree with surface observations from the NOAA network (see auxiliary material, Figures S4, S5, and S6).[1]

[9] The statistical uncertainty of individual $V_{meas}(CH_4)/V_{meas}(CO_2)$ retrievals is estimated 1.8% on average [*Frankenberg et al.*, 2006]. Potential systematic errors of the retrievals and the applied CO_2 correction are discussed in section 4.5.

[10] Individual SCIAMACHY pixels are 30 km $\times$ 60 km (for the applied channel 6). In this study, we average the original SCIAMACHY data on a regular 1° longitude $\times$ 1° latitude grid. SCIAMACHY achieves global coverage every six days (14 orbits per day); however, the density of valid data strongly depends on clouds, latitude, season, and surface (land versus ocean). As in *Frankenberg et al.* [2006], we apply a relatively strict cloud filter discarding measurements with an effective cloud top height of more than 1 km.

[11] The sensitivity of SCIAMACHY retrievals as functions of altitude are described by the averaging kernel (AK) [*Frankenberg et al.*, 2006]. The AKs are close to 1.0 near the surface and in the lower troposphere, but decrease in the upper troposphere and stratosphere. Furthermore, the AK depends on the air mass factor (AMF) of the corresponding retrieval, with larger AMFs leading to a stronger decrease of AKs with altitude. The AMF is defined as the ratio of the total observed slant column (incident and reflected solar radiation, as illustrated by *Frankenberg et al.* [2006, Figure 1]) to the (single) vertical column. AMFs are ranging between 2 to 4 in the retrievals; pixels with greater AMFs are excluded.

[12] We apply a constant scaling factor of 0.980 for the retrieved $\overline{VMR}(CH_4)$ for better visual comparability with model simulations. In the coupled inversion this scaling factor results in an average bias correction (see section 3.4) close to zero (global annual mean).

[13] Throughout this paper we use the terms SCIAMACHY CH_4 "retrievals," "measurements," and "observations" synonymously, but emphasize that these terms always refer to the particular CH_4 product as described above (including CO_2 correction based on TM3 model simulations).

2.2. Ground-Based Measurements

[14] Surface observations of CH_4 mixing ratios are from the NOAA ESRL (formerly CMDL) global cooperative air sampling network [*Dlugokencky et al.*, 2003, 1994]. Measurement sites are compiled in Table 1 and illustrated in Figure 1. We use only marine and continental background sites in the inversion. Sites that are significantly influenced by regional sources (e.g., BAL, BSC) were omitted to minimize potential systematic errors due to the so-called aggregation error [*Kaminski et al.*, 2001]. Furthermore, we omit some sites that are difficult to simulate with the $6^\circ \times 4^\circ$ coarse grid version of the TM5 model (see section 3.1), e.g., sites at the land-sea border [*Peters et al.*, 2004]. Only flask measurements are used for the inversion. The major reason not to include data from the few continuous measurement sites is to avoid further complication due to the different weighting of data with very different temporal resolution (see also section 3.4). Measurements are relative

[1] Auxiliary materials are available in the HTML. doi:10.1029/2006JD007268.

Table 1. Surface Air Sampling Sites From the NOAA Network[a]

ID	Station Name	Latitude, °	Longitude, °	Altitude, m asl	INV
ALT	Alert, Nunavut, Canada	82.45	−62.52	210	•
ZEP	Ny-Alesund, Svalbard (Spitsbergen), Norway and Sweden	78.90	11.88	474	•
SUM	Summit, Greenland	72.58	−38.48	3238	•
BRW	Barrow, Alaska, USA	71.32	−156.60	11	•
PAL	Pallas, Finland	67.97	24.12	560	
STM	Ocean station M, Norway	66.00	2.00	7	•
ICE	Heimay, Vestmannaeyjar, Iceland	63.25	−20.15	100	•
BAL	Baltic Sea, Poland	55.50	16.67	7	
CBA	Cold Bay, Alaska, USA	55.20	−162.72	25	•
MHD	Mace Head, Ireland	53.33	−9.90	25	
SHM	Shemya Island, Alaska, USA	52.72	174.10	40	•
LEF	Park Falls, Wisconsin, USA	45.93	−90.27	868	
KZD	Sary Taukum, Kazakhstan	44.45	77.57	412	
UUM	Ulaan Uul, Mongolia	44.45	111.10	914	•
BSC	Black Sea, Constanta, Romania	44.17	28.68	3	
KZM	Plateu Assy, Kazakhstan	43.25	77.88	2519	•
NWR	Niwot Ridge, Colorado, USA	40.05	−105.58	3475	•
UTA	Wendover, Utah, USA	39.90	−113.72	1320	
PTA	Point Arena, California, USA	38.95	−123.73	17	
AZR	Terceira Island, Azores, Portugal	38.77	−27.38	40	•
TAP	Tae-ahn Peninsula, Republic of Korea	36.73	126.13	20	
WLG	Mt. Waliguan, Peoples Republic of China	36.29	100.90	3810	•
BME	St. Davis Head, Bermuda, UK	32.37	−64.65	30	
BMW	Tudor Hill, Bermuda, UK	32.27	−64.88	30	•
WIS	Sede Boker, Negev Desert, Israel	31.13	34.88	400	
IZO	Tenerife, Canary Islands, Spain	28.30	−16.48	2360	•
MID	Sand Island, Midway, USA	28.22	−177.37	4	•
KEY	Key Biscayne, Florida, USA	25.67	−80.20	3	
ASK	Assekrem, Algeria	23.18	5.42	2728	•
MLO	Mauna Loa, Hawai, USA	19.53	−155.58	3397	•
KUM	Cape Kumukahi, Hawaii, USA	19.52	−154.82	3	•
GMI	Mariana Islands, Guam	13.43	144.78	2	•
RPB	Ragged Point, Barbados	13.17	−59.43	45	•
CHR	Christmas Island, Republic of Kiribati	1.70	−157.17	3	•
SEY	Mahe Island, Seychelles	−4.67	55.17	3	•
ASC	Ascension Island, UK	−7.92	−14.42	54	•
SMO	Tutuila, American Samoa, USA	−14.23	−170.57	42	•
NMB	Gobabeb, Namibia	−23.57	15.03	408	
EIC	Easter Island, Chile	−27.15	−109.45	50	•
CGO	Cape Grim, Tasmania, Australia	−40.68	144.68	94	
CRZ	Crozet Island, France	−46.45	51.85	120	•
TDF	Tierra Del Fuego, La Redonda Isla, Argentinia	−54.87	−68.48	20	•
PSA	Palmer Station, Antarctica, USA	−64.92	−64.00	10	•
SYO	Syowa Station, Antarctica, Japan	−69.00	39.58	11	•
HBA	Halley Station, Antarctica, UK	−75.58	−26.50	10	•
SPO	South Pole, Antarctica, USA	−89.98	−24.80	2810	•

[a]The last column (“INV”) indicates the sites used for the inversions.

to the new NOAA04 scale [*Dlugokencky et al.*, 2005], which is based on gravimetrically prepared standards. This new scale is a factor of (1.0124 ± 0.0007) greater than the previously used CMDL83 scale.

3. Modeling

3.1. TM5 Model

[15] We use the two-way nested atmospheric zoom model TM5 [*Krol et al.*, 2005]. TM5 is an offline transport model that uses meteorological fields from the ECMWF IFS model (6-hourly forecast, based on 4D-VAR analyses) [*ECMWF*, 2002]. We employ the tropospheric standard version of TM5 with 25 vertical layers, which are defined as a subset of the 60 layers of the operational ECMWF model. This TM5 version has been intensively validated and compared with other transport models using the atmospheric tracers ^{222}Rn and SF_6 [*Bergamaschi et al.*, 2006].

[16] The base functions used for the inversion (see section 3.4) were simulated at global resolution of 6° × 4°. After obtaining the a posteriori emissions from the inversion, TM5 is rerun at higher resolution, using a multiple zoom region version of TM5 with global resolution of 3° × 2° and six zoom regions, simulated at 1° × 1°, over major continental areas: North America, South America, Europe, Africa, Asia, and Australia. The extension of these zoom regions is illustrated in Figure 1. Global simulations at 6° × 4° (base functions) and 3° × 2° (final global simulations) are interpolated bi-linearly to a 1° × 1° grid.

[17] Chemical destruction of CH_4 by OH radicals is simulated using precalculated OH fields based on CBM-4 chemistry [*Houweling et al.*, 1998] and optimized with methyl chloroform [*Bergamaschi et al.*, 2005]. Chemical destruction of CH_4 by OH, Cl and $O(^1D)$ radicals in the stratosphere are based on the 2-D photochemical Max-Planck-Institute (MPI) model [*Bergamaschi et al.*, 2005; *Brühl and Crutzen*, 1993].

[18] For comparison with SCIAMACHY column-averaged mixing ratios, we apply the corresponding aver-

Table 2. A Priori Bottom-Up Inventories and a Priori Annual Total Emissions

Source Category	Reference	Emission, Tg CH_4/yr
Coal mining	IIASA[a] [*Klaassen et al.*, 2004]	26.6
Oil and natural gas	IIASA[a] [*Klaassen et al.*, 2004]	50.6
Enteric fermentation	IIASA[a] [*Klaassen et al.*, 2004]	99.6
Rice	GISS [*Matthews et al.*, 1991]	59.7
Biomass burning	[*van der Werf et al.*, 2004]	23.6
Waste	IIASA[a] [*Klaassen et al.*, 2004]	69.7
Wetlands	(1) as described in section 3.3 (2) [*Walter et al.*, 2001a, 2001b]	174.5
Wild animals	[*Houweling et al.*, 1999]	5.0
Termites	[*Sanderson*, 1996]	19.2
Soil	[*Ridgwell et al.*, 1999]	−37.8
Ocean	[*Houweling et al.*, 1999]	17.0

[a]IIASA inventory has been spatially disaggregated on 1° × 1° [*Dentener et al.*, 2005] using the EDGAR 3.2 database for year 1995 [*Olivier and Berdowski*, 2001].

aging kernels of the retrievals to the TM5 model output (see also section 2.1 and *Frankenberg et al.* [2006]). Thus the column averaged mixing ratio of the model output $\overline{VMR}_{TM5}$ is calculated as:

$$\overline{VMR}_{TM5} = \frac{1}{p_{tot}} \sum_{l} \left[VMR_a^l + AK^l \cdot \left(VMR_{TM5}^l - VMR_a^l \right) \right] \Delta p^l \tag{2}$$

where l is the index of the vertical layer, AK^l the averaging kernel, VMR_a^l the a priori mixing ratio (applied in the retrieval) and VMR_{TM5}^l the simulated mixing ratio of layer l. Δp^l is the pressure difference between upper and lower boundary of layer l and p_{tot} is the total pressure of the column (= surface pressure). Due to the shape of AKs, the application of equation (2) leads to less weighting of the upper layers of the atmosphere. Model output is extracted close to the local equator crossing time of SCIAMACHY (approximately 10:00 LT).

3.2. Bottom-Up Inventories

[19] Bottom-up inventories used as a priori estimates of emissions are compiled in Table 2. For several anthropogenic source categories the International Institute for Applied System Analysis (IIASA) emission inventory was used for year 2003, based on the Regional Air Pollution Information and Simulation (RAINS) model, which has recently been extended to include GHGs [*Klaassen et al.*, 2004]. This inventory reports national annual totals and has been spatially disaggregated on 1° × 1° [*Dentener et al.*, 2005] using the EDGAR 3.2 database for 1995 [*Olivier and Berdowski*, 2001]. For biomass burning the Global Fire Emissions Database (GFED) version 1 [*van der Werf et al.*, 2004] was applied, using a multiannual average for the period 1997–2002. CH_4 emissions from wetlands are based, alternatively, on two different inventories: (1) a new inventory developed by one of the coauthors (J. O. Kaplan) which is described in more detail in section 3.3 and denoted 'JK'; (2) the wetland inventory of *Walter and Heimann* [2000] and *Walter et al.* [2001a, 2001b], using a multiyear average over 1982–1993. This inventory is denoted 'BW'. In both cases, the total annual wetland emissions are scaled to 175 Tg CH_4/yr. The total a priori bottom-up inventory is illustrated in Figure 3 (top) for the 'JK' case, aggregated to 6° × 4° resolution (which is the resolution of the base functions used for the inversion).

3.3. New Wetland Map and CH_4 Emission Model

[20] Because of known inconsistencies in available data sets of global wetland area and the availability of new, high-resolution land cover maps (including wetland classification) for certain continents, we compiled an original map of global wetlands. The map was assembled using the best available source of large-scale wetland cover information for each continent or region. While several of the data sets contained subclassifications of wetland type (e.g., bog, fen, forested wetland, or floodplain), it was not possible to create a globally consistent data set containing more information than simple presence or absence of wetland. Some data sets were vector polygon products while others were raster maps at resolutions from 30 m to 5′ (∼10 km). To create the global data set, we calculated the fractional cover of wetland area on a global 0.5° geographic grid. We used five major data sources to assemble the global wetland map. For Canada we used the vector Canadian Peatlands Database [*Tarnocai et al.*, 2000], rasterizing the map at 1 km resolution and aggregating fractional wetland cover to a 0.5° grid. For the conterminous United States we used the 30 m U.S. National Land Cover Dataset [*Vogelmann et al.*, 2001]. Data for South America, Africa, Eastern Europe, and northern Asia come from the 1 km native resolution GLC2000 global land cover data set [*JRC*, 2003]. Data for Europe is from the 250 m CORINE90 Land Cover data set [*ETCTE*, 2000]. For all other regions we used the 5′ WELAREM1 database of global wetlands [*Lehner and Döll*, 2001].

[21] To estimate methane emissions from global wetlands, we adapted the simple scheme used by *Christensen et al.* [1996] and *Kaplan* [2002] to the Lund-Potsdam-Jena Dynamic Global Vegetation Model (LPJ DGVM) [*Sitch et al.*, 2003]. Fundamentally, gross wetland methane production simulated by the model depends on three factors: the availability of labile substrate for methanogenesis, soil temperature, and water table depth. These quantities are represented in the LPJ DGVM model as total soil respiration rate, which integrates the fast-turnover soil organic matter pool and soil temperature, and as soil moisture, which is a proxy for water table depth. The resulting model

Table 3. Inversion Scenarios, a Priori and a Posteriori Emissions, and Their Uncertainties

		a Priori		S1	S2	S3	S4	S5	S6
Source	Region[a]	JK[b]	BW[b]	JK[b] Surface[c] 1.00[d]	BW[b] Surface[c] 1.00[d]	JK[b] Surface + SCIA[c] 1.00[d]	BW[b] Surface + SCIA[c] 1.00[d]	JK[b] Surface + SCIA[c] 0.95[d]	JK[b] Surface + SCIA[c] 1.05[d]
Coal	NH1	3.7 ± 1.5		4.3 ± 1.5	4.6 ± 1.4	5.1 ± 1.4	5.3 ± 1.4	5.1 ± 1.4	5.1 ± 1.4
	NH2	5.1 ± 2.1		4.9 ± 2.0	5.0 ± 2.0	6.4 ± 1.9	6.4 ± 1.9	6.6 ± 1.9	6.3 ± 1.9
	NH3	11.1 ± 4.6		13.4 ± 3.8	13.8 ± 3.7	19.7 ± 3.3	20.4 ± 3.3	20.1 ± 3.3	19.4 ± 3.3
	SH	6.8 ± 2.8		8.9 ± 2.3	5.4 ± 2.3	4.3 ± 1.8	0.0 ± 1.8	4.0 ± 1.8	4.7 ± 1.8
	GLOBAL	**26.6 ± 6.0**		**31.5 ± 5.0**	**28.7 ± 5.0**	**35.6 ± 4.4**	**32.1 ± 4.3**	**35.8 ± 4.4**	**35.5 ± 4.4**
Oil and gas	NH1	3.4 ± 1.4		4.9 ± 1.2	5.0 ± 1.2	5.2 ± 1.2	5.2 ± 1.2	5.1 ± 1.2	5.3 ± 1.2
	NH2	27.8 ± 11.5		26.5 ± 7.6	26.1 ± 7.4	16.0 ± 5.2	10.9 ± 5.2	16.1 ± 5.2	16.1 ± 5.2
	NH3	16.1 ± 6.7		8.9 ± 4.0	10.8 ± 3.7	16.6 ± 3.6	18.9 ± 3.4	18.0 ± 3.6	16.4 ± 3.6
	SH	3.3 ± 1.4		3.4 ± 1.4	3.1 ± 1.4	4.0 ± 1.3	2.8 ± 1.4	3.7 ± 1.3	4.3 ± 1.3
	GLOBAL	**50.6 ± 13.5**		**43.7 ± 7.2**	**45.0 ± 7.0**	**41.8 ± 5.5**	**37.8 ± 5.5**	**42.9 ± 5.5**	**42.0 ± 5.5**
Ent. ferm.	NH1	15.3 ± 3.8		17.1 ± 3.4	21.1 ± 3.4	19.0 ± 3.2	23.3 ± 3.2	18.1 ± 3.2	19.8 ± 3.2
	NH2	25.9 ± 6.4		23.6 ± 5.6	22.3 ± 5.7	27.1 ± 5.2	24.1 ± 5.3	25.9 ± 5.2	28.1 ± 5.2
	NH3	37.5 ± 9.3		30.7 ± 7.8	31.3 ± 7.7	10.6 ± 6.3	12.7 ± 6.3	10.9 ± 6.3	10.2 ± 6.3
	SH	20.8 ± 5.2		25.6 ± 3.9	18.2 ± 4.1	25.3 ± 3.5	15.3 ± 3.8	23.7 ± 3.5	27.0 ± 3.5
	GLOBAL	**99.6 ± 13.0**		**97.1 ± 10.9**	**92.9 ± 10.9**	**82.0 ± 9.6**	**75.4 ± 9.7**	**78.6 ± 9.6**	**85.2 ± 9.6**
Rice	NH1	1.1 ± 0.2		1.1 ± 0.2	1.1 ± 0.2	1.1 ± 0.2	1.1 ± 0.2	1.1 ± 0.2	1.1 ± 0.2
	NH2	1.9 ± 0.4		1.9 ± 0.4	1.9 ± 0.4	1.9 ± 0.4	1.8 ± 0.4	1.8 ± 0.4	1.9 ± 0.4
	NH3	49.6 ± 8.8		52.9 ± 6.6	51.8 ± 6.4	37.9 ± 4.9	44.7 ± 4.5	38.2 ± 4.9	37.7 ± 4.9
	SH	7.3 ± 1.3		7.5 ± 1.3	7.1 ± 1.3	7.8 ± 1.2	6.5 ± 1.2	7.6 ± 1.2	8.0 ± 1.2
	GLOBAL	**59.7 ± 8.9**		**63.4 ± 6.7**	**61.8 ± 6.5**	**48.7 ± 5.1**	**54.0 ± 4.7**	**48.7 ± 5.1**	**48.7 ± 5.1**
Bio. burn.	EXNH	1.1 ± 0.4		1.2 ± 0.4	1.2 ± 0.4	1.3 ± 0.4	1.4 ± 0.4	1.2 ± 0.4	1.3 ± 0.4
	TR1	8.7 ± 2.6		8.8 ± 2.2	11.0 ± 2.2	9.6 ± 1.8	12.9 ± 1.7	9.4 ± 1.8	9.9 ± 1.8
	TR2	9.7 ± 2.5		10.0 ± 2.1	9.8 ± 2.1	7.8 ± 1.8	8.8 ± 1.8	7.8 ± 1.8	7.7 ± 1.8
	TR3	3.8 ± 1.1		3.4 ± 1.1	3.7 ± 1.1	3.0 ± 1.0	2.7 ± 1.0	2.8 ± 1.0	3.2 ± 1.0
	EXSH	0.2 ± 0.1		0.2 ± 0.1	0.2 ± 0.1	0.2 ± 0.1	0.2 ± 0.1	0.2 ± 0.1	0.2 ± 0.1
	GLOBAL	**23.6 ± 3.8**		**23.6 ± 3.1**	**26.0 ± 3.1**	**21.9 ± 2.6**	**26.1 ± 2.6**	**21.5 ± 2.6**	**22.2 ± 2.6**
Waste	NH1	10.8 ± 4.5		11.6 ± 3.7	15.8 ± 3.6	11.0 ± 3.4	12.2 ± 3.4	9.7 ± 3.4	12.3 ± 3.4
	NH2	17.3 ± 7.2		15.8 ± 6.1	15.3 ± 6.0	18.2 ± 5.6	15.2 ± 5.6	17.5 ± 5.6	18.7 ± 5.6
	NH3	33.7 ± 14.0		34.6 ± 9.8	42.7 ± 9.7	25.2 ± 8.3	23.9 ± 8.3	22.0 ± 8.3	27.8 ± 8.3
	SH	7.9 ± 3.3		10.4 ± 3.1	8.6 ± 3.2	12.5 ± 3.1	10.8 ± 3.1	11.6 ± 3.1	13.5 ± 3.1
	GLOBAL	**69.7 ± 16.7**		**72.4 ± 12.0**	**82.5 ± 11.8**	**67.0 ± 10.7**	**62.0 ± 10.7**	**60.8 ± 10.7**	**72.3 ± 10.7**
Wetlands	EXNH1	32.5 ± 9.1	11.7 ± 4.2	22.3 ± 2.7	12.9 ± 1.7	23.4 ± 2.1	14.1 ± 1.4	23.3 ± 2.1	23.3 ± 2.1
	EXNH2	8.9 ± 2.3	19.6 ± 6.7	3.2 ± 1.3	9.5 ± 2.7	3.6 ± 1.2	8.9 ± 2.0	3.8 ± 1.2	3.4 ± 1.2
	EXNH3	18.5 ± 5.7	14.6 ± 5.5	17.0 ± 2.7	16.0 ± 2.7	19.0 ± 2.1	18.1 ± 2.0	18.7 ± 2.1	19.0 ± 2.1
	TR1	49.9 ± 12.1	42.9 ± 10.2	63.0 ± 6.0	62.5 ± 7.1	66.9 ± 3.5	62.4 ± 4.4	64.4 ± 3.5	69.4 ± 3.5
	TR2	24.4 ± 5.8	42.1 ± 9.8	31.2 ± 4.5	35.9 ± 6.0	47.1 ± 3.0	44.8 ± 3.9	46.0 ± 3.0	48.4 ± 3.0
	TR3	38.6 ± 9.2	38.9 ± 9.1	44.2 ± 7.0	39.1 ± 6.3	46.8 ± 4.2	42.2 ± 3.7	43.0 ± 4.2	50.6 ± 4.2
	EXSH	1.8 ± 0.5	4.7 ± 1.2	1.9 ± 0.5	3.8 ± 1.2	1.8 ± 0.4	1.5 ± 1.1	1.8 ± 0.4	1.8 ± 0.4
	GLOBAL	**174.6 ± 19.6**	**174.4 ± 19.4**	**182.7 ± 9.4**	**179.5 ± 10.0**	**208.5 ± 7.6**	**192.1 ± 8.0**	**201.1 ± 7.6**	**215.8 ± 7.6**
Wild animals	**GLOBAL**	**5.0 ± 2.1**		**6.5 ± 2.0**	**6.3 ± 2.0**	**6.8 ± 2.0**	**7.3 ± 2.0**	**6.7 ± 2.0**	**7.0 ± 2.0**
Termites	**GLOBAL**	**19.2 ± 8.0**		**30.6 ± 7.0**	**32.3 ± 7.2**	**42.0 ± 6.7**	**67.2 ± 6.7**	**38.2 ± 6.7**	**46.0 ± 6.7**
Soil	**GLOBAL**	**−37.8 ± 6.4**		**−29.8 ± 6.0**	**−32.9 ± 6.0**	**−21.3 ± 5.8**	**−20.6 ± 5.8**	**−23.6 ± 5.8**	**−18.8 ± 5.8**
Ocean	**GLOBAL**	**17.0 ± 7.0**		**1.9 ± 3.2**	**0.8 ± 3.1**	**−1.3 ± 2.9**	**0.6 ± 2.8**	**−1.9 ± 2.9**	**−1.3 ± 2.9**
Total	**GLOBAL**	**507.7 ± 36.0**		**523.5 ± 4.4**	**522.9 ± 5.1**	**531.6 ± 3.7**	**533.9 ± 4.2**	**508.8 ± 3.7**	**554.4 ± 3.7**

Table 3. (continued)

		a Priori		S1	S2	S3	S4	S5	S6
Source	Region[a]	JK[b]	BW[b]	JK[b] Surface[c] 1.00[d]	BW[b] Surface[c] 1.00[d]	JK[b] Surface + SCIA[c] 1.00[d]	BW[b] Surface + SCIA[c] 1.00[d]	JK[b] Surface + SCIA[c] 0.95[d]	JK[b] Surface + SCIA[c] 1.05[d]
Surface observations									
N				**1816**	**1805**	**1806**	**1799**	**1804**	**1805**
X^2(a priori)[e]				**10.3**	**3.4**	**10.6**	**3.6**	**9.8**	**14.5**
X^2(a posteriori)[e]				**1.2**	**1.2**	**1.3**	**1.3**	**1.3**	**1.3**
SCIAMACHY observations									
N						**15365**	**15364**	**15364**	**15365**
X^2(a priori)[e]						**0.93**	**0.80**	**0.86**	**1.09**
X^2(a posteriori)[e]						**0.46**	**0.48**	**0.47**	**0.46**

[a]For definition of regions, see Figure 2.
[b]Applied wetland inventory (see sections 3.2 and 3.3).
[c]Observations used for the inversion.
[d]Global OH scaling (see section 4.3).
[e]Chi-square, defined as $X^2 = \frac{1}{n}\sum_{i=1}^{n}\frac{[CH_{4,\mathrm{model},i} - CH_{4\,\mathrm{data},i}]^2}{\Delta CH_{4\,\mathrm{data},i}^2}$, is given for a priori and a posteriori model simulations (separately for surface and SCIAMACHY data).

emphasizes the temperature control on methane production in high-latitude wetlands and moisture control in tropical wetlands. Net CH_4 emissions are reduced relative to gross production as a function of overlying vegetation cover to account for oxidation of methane in some plant communities, e.g., in forested peatlands.

[22] This extended version of the LPJ DGVM is driven by time series of monthly mean temperature and cloud fraction and monthly total precipitation. Using this model, we simulated methane emissions from wetlands during 1991–2000. To first initialize the soil carbon pool, we prepared a driver data set by linearly detrending a 0.5° globally gridded time series of 20th century climate [*Mitchell and Jones*, 2005; *New et al.*, 2002]. We ran LPJ for 1000 years by repeating the climate time series in 100 year cycles. After this spin-up, we used the original 20th century gridded climate time series to run the model for the period 1901–2000. We stored monthly model output for the last decade of this run and apply the average values in this study. In the following, this CH_4 wetland emission inventory is denoted 'JK'. A more detailed description of the wetland map and emission model will be described elsewhere.

3.4. Inversion Technique

[23] We use a synthesis inversion approach, describing the total CH_4 mixing ratio $\overrightarrow{VMR}_{\mathrm{mod}}(\vec{p}, \vec{x}, t)$ as a linear combination of n_{para} base functions $\overrightarrow{VMR}_{\mathrm{mod},i}(\vec{x}, t)$:

$$\overrightarrow{VMR}_{\mathrm{mod}}(\vec{p},\vec{x},t) = \sum_{i=1}^{n_{para}} p_i \overrightarrow{VMR}_{\mathrm{mod},i}(\vec{x},t) \tag{3}$$

with scaling factors p_i (summarized as vector $\vec{p}$). n_{para} is the total number of parameters to be optimized (see below). Technically, this approach is very similar to that described by *Bergamaschi et al.* [2005]. However, instead of solving for emissions only by region, we separate emissions based on source categories and large spatial regions. The 11 source categories considered are compiled in Tables 2 and 3. Most anthropogenic source categories (coal mining, oil and natural gas, enteric fermentation, waste, and rice) are subdivided each into four large global regions: three in the NH, and one for the SH (Figure 2, top). Wetland emissions are separated into seven global regions, with three regions in the extratropical NH, three regions in the tropics and one region for the extratropical SH (Figure 2, middle). Biomass burning is subdivided into five regions, including three separate tropical regions (Figure 2, bottom). For some minor natural sources (wild animals, termites, soil, and ocean), no further spatial separation has been applied. In total, 36 different categories/regions are applied.

[24] The definition of the cost function, calculation of optimized (a posteriori) emissions and calculation of a posteriori covariance matrix are as described by *Bergamaschi et al.* [2005]. The OH sink (see section 3.1) is included in the individual base functions. We optimize monthly mean emissions, which allows optimization of seasonal cycles. For source categories for which significant seasonal variations are unlikely (coal mining, oil and natural gas, enteric fermentation, waste, wild animals, termites, and ocean), however, we specify a high temporal correlation (r = 0.9) for emissions of consecutive months in the a priori covariance matrix. In contrast, this correlation has been set to zero

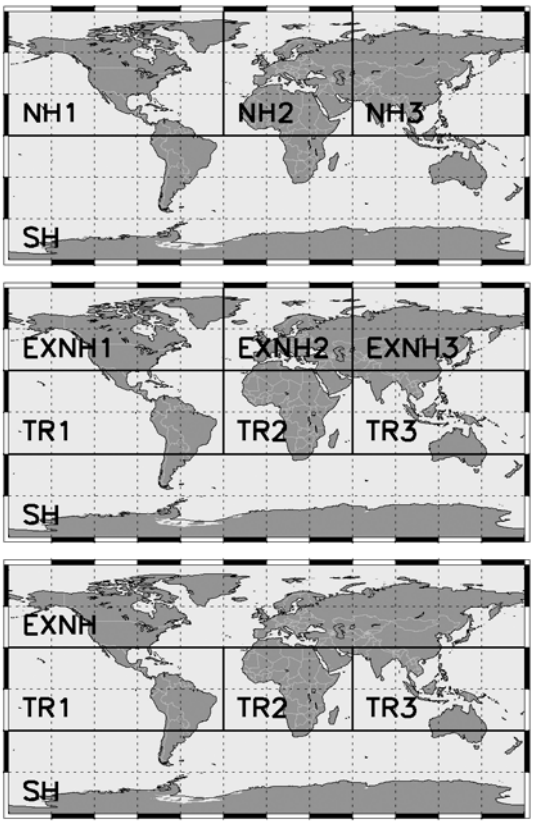

Figure 2. Definition of regions for the base functions for different source categories (see section 3.4 and Table 3).

for the source categories with large variations (wetlands, rice paddies, biomass burning). For most categories we assume an uncertainty of 50% per region and month. For enteric fermentation a smaller uncertainty of 30% is assumed, and for wetlands and biomass burning we use a higher uncertainty of 80% (per region and month). The resulting overall uncertainties for the annual totals (considering also the specified correlations between consecutive months) are listed in Table 3.

[25] This study is analyzing the year 2003. Global CH_4 mixing ratios have been initialized using results of a previous inversion. Furthermore, we introduce two spin-up months prior to year 2003 (in order to allow some adaptation to potential errors of the initialization) and simulate also January 2004 (to account for the delayed influence of emissions on observations). The total number of base functions, n_{para}, is 36 (categories/regions) $\times$ 15 (months) + 1 (base function for further development of initial state (at 1 November 2002)) = 541.

[26] As we show in section 4.1, SCIAMACHY data may have some bias dependent on latitude and season. In the inversions that simultaneously use surface measurements and SCIAMACHY data (scenarios S3–S6; see section 3.5), we allow for this bias using polynomials as function of latitude (y) and month (but independent of longitude x):

$$VMR_{SCIAMACHY,corrected}(x,y,t) = VMR_{SCIAMACHY}(x,y,t) - \sum_{n=0}^{2} a_n(t) y^n \quad (4)$$

with the coefficients a_n determined by the inversion. No a priori constraints are applied for these coefficients.

[27] Measurement uncertainty is assumed to be ±3 ppb for surface measurements. In addition, we include also an estimate of the representativeness error, based on the 3D model gradient, as described in *Bergamaschi et al.* [2005]. The uncertainty of SCIAMACHY column averaged mixing ratios is assumed to be ±1.5%. While the calculated statistical uncertainty is typically very small for monthly aggregated values ($\ll$1%, scaling with $\sim 1/\sqrt{n}$ for random errors [*Frankenberg et al.*, 2006]), we assume the specified constant overall uncertainty of ±1.5% for all SCIAMACHY data in this study in order to account for systematic errors (see also section 4.5).

[28] Surface measurements are treated as daily means, SCIAMACHY measurements as monthly composites (and sampled in the model on those days for which valid measurements exist). Since we are optimizing monthly emissions, we apply a weighting factor α_i = 1/4 for the individual daily surface data. This weighting factor is implemented by increasing the effective data uncertainty ($\alpha_i < 1$) [*Bergamaschi et al.*, 2005]:

$$\left[\Delta CH_{4\,data,i}\right]^2 \rightarrow \frac{1}{\alpha_i}\left[\Delta CH_{4\,data,i}\right]^2 \quad (5)$$

No weighting factor is applied for the monthly satellite data. The inversion is performed in two iterations, rejecting outliers for which observational data differ from inverse model simulations of the first iteration by more than 3 σ [*Bergamaschi et al.*, 2005].

3.5. Inversion Scenarios

[29] We present six different inversion scenarios (Table 3). The first two scenarios, S1 and S2, are based on the surface measurements from the NOAA network only. In S1, the 'JK' wetland inventory is used, while in S2 the 'BW' wetland inventory is employed. Scenarios S3–S6 are based on the combined use of surface and SCIAMACHY measurements. S3 is analogous to S1, using the 'JK' inventory, and S4 analogous to S2, using the 'BW' inventory. Scenarios S5 and S6 investigate the influence of the OH sink: In S5 the OH sink is globally reduced by 5%, and in S6 the OH sink is increased by 5%; otherwise scenarios S5 and S6 are identical to S3. Technically this is done by adding an additional base function in equation (3) which describes the OH perturbation, since the source base functions already contain the 'regular' OH sink [see also *Bergamaschi et al.*, 2005].

4. Results and Discussion

4.1. Comparison of SCIAMACHY Measurements With Inverse Simulations Based on NOAA Surface Measurements

[30] Our base scenario S1 leads to relatively small changes per source category compared to the a priori estimates (Table 3). However, significant redistribution between regions is calculated particularly for CH_4 emissions from wetlands, with total emissions from NH extratropical regions (30–90°N) decreasing from 59.9 to 42.5 Tg CH_4/yr, and total emissions from tropical regions increasing from

112.9 to 138.4 Tg CH_4/yr. At the same time, an increase of CH_4 from termites (with assumed emissions mainly in the tropics) and a small decrease of the soil sink (which is assumed to be largest in the tropics) is calculated, further increasing overall tropical net emissions. The spatial redistribution of CH_4 sources is further illustrated in Figure 3, which shows increased emissions in tropical regions of South America and Africa, and decreased emissions in the Hudson Bay Lowlands and Siberia. Furthermore, the figure shows a tendency to decrease NH emissions and increase SH emissions, enforced by the inversion, to correctly simulate the observed NS gradient.

[31] Figure 4 shows observations and inverse model simulation (for scenario S1) at key sampling sites. The figure illustrates that major features of the observed CH_4 distribution at the surface are reproduced well by the model simulations. This is true of both the NS gradient and the seasonal variations at most sites (within the assumed uncertainties of measurements and model simulations (representativeness error)). Furthermore, synoptic scale variations are simulated rather well at most sites. The complete set of NOAA sites is shown in the auxiliary material, also highlighting the contribution from the individual base functions (Figure S7). From this favorable agreement between inverse model simulations and observations at background sites we conclude that the model fields constitute a good reference for comparison with SCIAMACHY retrievals over remote regions. In section 4.5 we show that potential systematic errors of model simulations in the vertical CH_4 distribution are likely to have an overall only relatively small impact to column averaged mixing ratios.

[32] Scenario S2, based on the 'BW' wetland inventory, also shows the general tendency of increasing tropical emission and decreasing extratropical emissions in the NH (Table 3). Despite significant differences in the spatial distribution of CH_4 emission from wetlands, simulations at the NOAA sites are very similar to scenario S1 (Figure S8). This is because most sites are not very sensitive to tropical wetland emissions, and the inversion is able to compensate for the differences in bottom-up inventories such that observations at remote sites can be reproduced with a similar level of agreement. This is also reflected in the virtually identical χ^2 of 1.2 for both scenarios (see Table 3). However, there are significant discrepancies between these two simulations directly over tropical source regions, particularly over South America (see below).

4.1.1. SCIAMACHY Versus TM5: Global Distribution

[33] Figure 5 shows 3-monthly composites for 2003 of the global SCIAMACHY measurements and the corresponding model simulations for scenario S1. Model data are sampled only at those pixels and days for which valid SCIAMACHY retrievals exist. The major features of both SCIAMACHY and TM5 global distributions are (1) the significant NS gradient, which is clearly apparent over the ocean and continental background regions, and (2) the elevated mixing ratios over source regions, in particular India, Southeast Asia, and tropical regions of South America and Africa.

[34] To quantitatively evaluate the agreement of the NS gradient between observations and model simulations, we show the latitudinal averages, separated into pixels over ocean and pixels over land (Figure 6). While the latitudinal averages over the ocean are largely representative for background conditions, the latitudinal averages over land pixels are significantly influenced by the CH_4 sources. It should be noted, though, that SCIAMACHY measurements over the ocean are restricted to conditions with either low lying clouds, Sun glint or a very rough ocean surface. Therefore, it cannot be ruled out that small systematic differences exist between the SCIAMACHY measurements over the ocean and over land. With the applied relatively restrictive cloud filter, however, this systematic effect appears to be relatively small [*Frankenberg et al.*, 2006].

[35] Over the ocean, we see rather good agreement of the NS gradient for the period January to March (Figures 5 and 6), while subsequent periods show systematic biases at some latitudes: In particular, between April and June SCIAMACHY retrievals are significantly lower ($\sim$20–30 ppb) than model simulation between 10 and 40°S. While the number of ocean pixels in this latitude region and season is rather small, the same tendency is also seen over landmasses, especially over Australia, which does not have large known CH_4 emissions and which therefore can be basically considered as continental background region. SCIAMACHY retrievals remain somewhat lower in this latitude region between July and September, but become slightly higher than model simulations between October and December.

[36] Over the ocean, some bias is also visible at high northern latitudes (70–90°N) between April and September, with SCIAMACHY retrievals being about 20 ppb lower than model simulations, while no comparison can be made for the high northern latitudes for January to March, and October to December, due to the lack of SCIAMACHY retrievals.

[37] While inverse model simulations over remote regions are rather insensitive for the two scenarios S1 and S2, the situation is very different over regions with strong emissions: Here the model simulations are strongly dominated by the patterns of the applied bottom-up inventories. Despite the optimization, major differences are possible, as the inversion is based on background sites only (for scenarios S1 and S2), and cannot optimize the spatial patterns within the predefined large regions (Figure 2). Major patterns over the continents are (1) the large CH_4 enhancements over tropical regions of South America and Africa, visible in both observations and model simulations, but with different spatial patterns during part of the year and the tendency of larger observed enhancements compared to simulations (visible also in the latitudinal average over land (Figure 6)), and (2) very large enhancements over India and Southeast Asia, most pronounced between April and September, and generally rather consistent between observations and model simulations.

[38] Furthermore, large CH_4 enhancements of SCIAMACHY retrievals are visible in Figure 5 over the northeastern United States, southern Canada, and large parts of Eurasia between $\sim$40°N and 60°N for the period January to March, while model simulations do not show such high values. However, in the representation of three monthly averages these high values originate from very few observations only (confined to March, while almost no data are available for January and February at these high latitudes; furthermore the scatter to these data is relatively large).

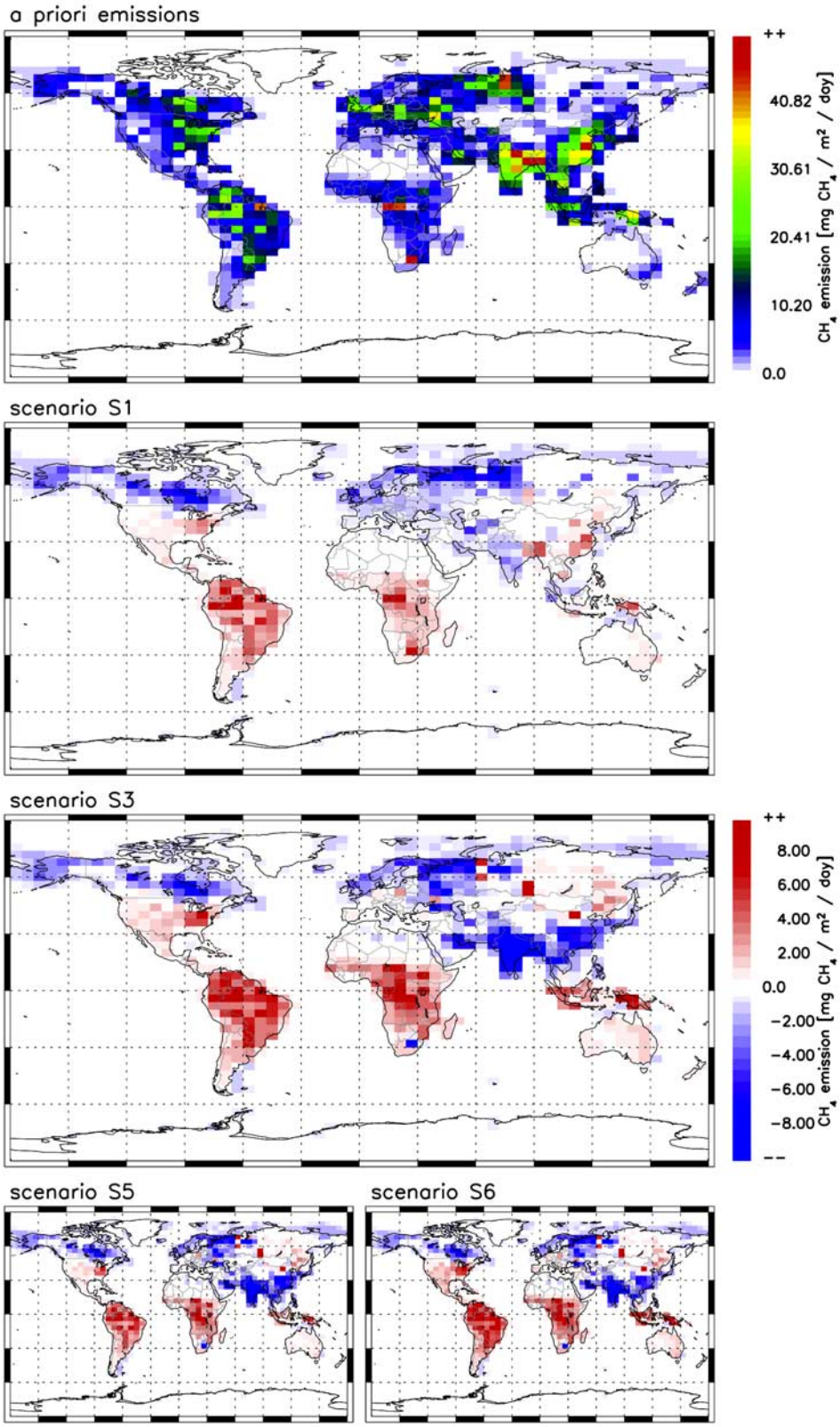

Figure 3. A priori emissions (top) and inversion increment for scenarios S1, S3, S5, and S6 (yearly mean values for 2003).

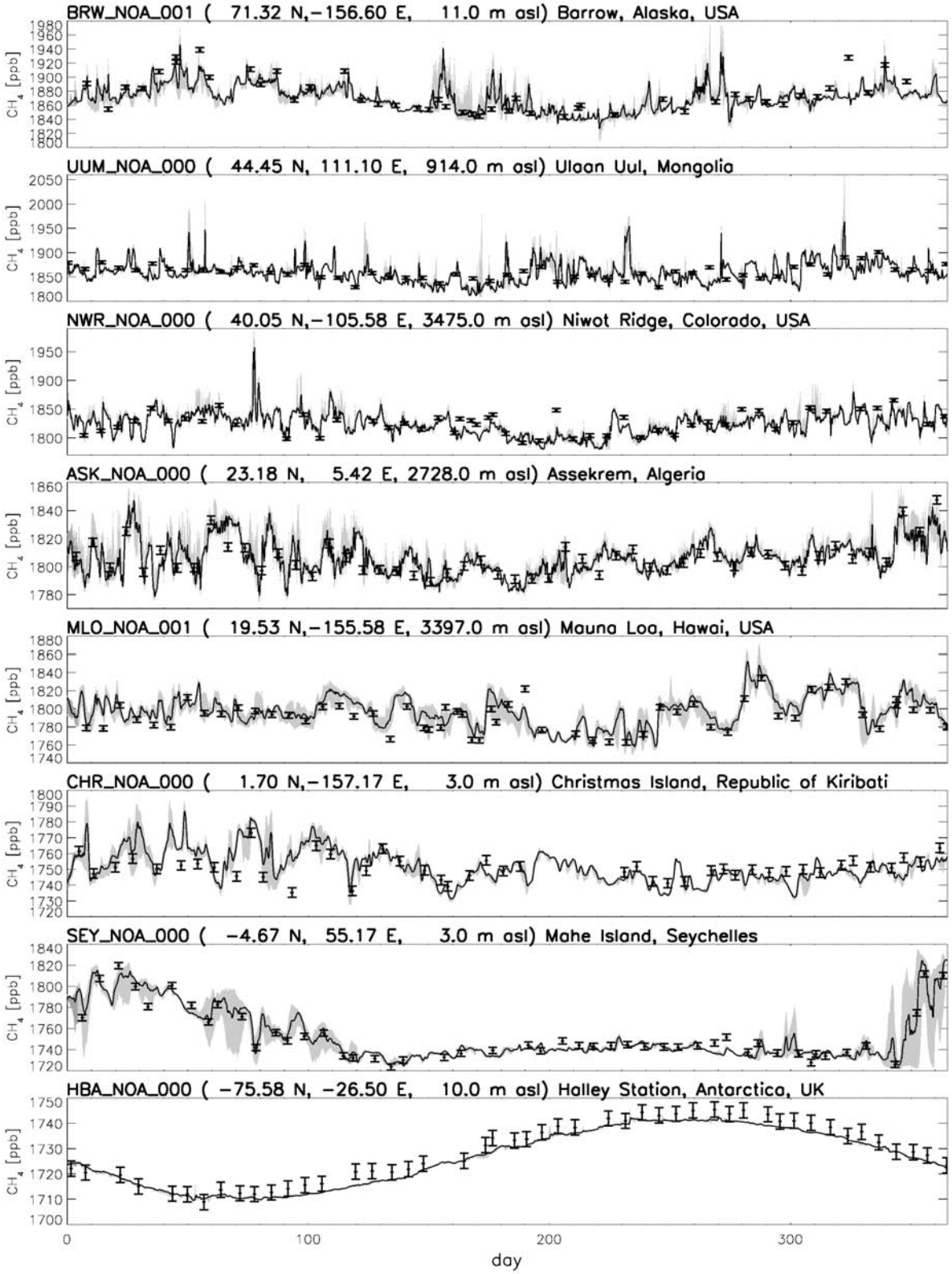

Figure 4. Comparison of model simulations for scenario S1 (solid curve) with observations (symbols) at eight NOAA air sampling sites during 2003. The grey shaded areas around the black solid curve show the estimated model representativeness error.

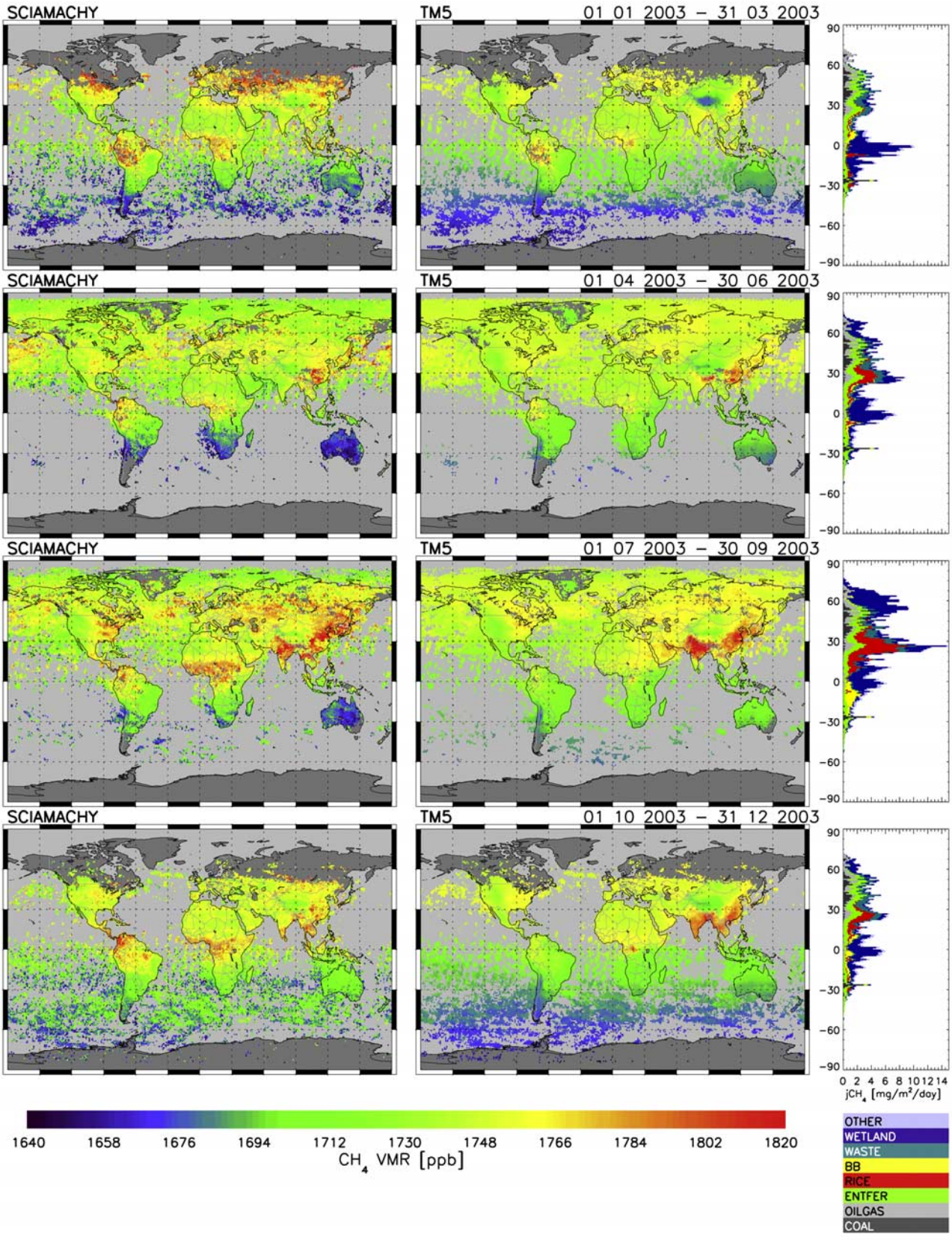

Figure 5. SCIAMACHY measurements (left) and TM5 simulations (right) for scenario S1. The far right panels show the contributions from different source categories (latitudinal average in mg $CH_4/m^2/day$). Each row shows a 3-month composite. Model data are sampled only at those pixels and days for which valid SCIAMACHY retrievals exist. Model simulations have been made at $3^\circ \times 2^\circ$ resolution, and are interpolated to $1^\circ \times 1^\circ$.

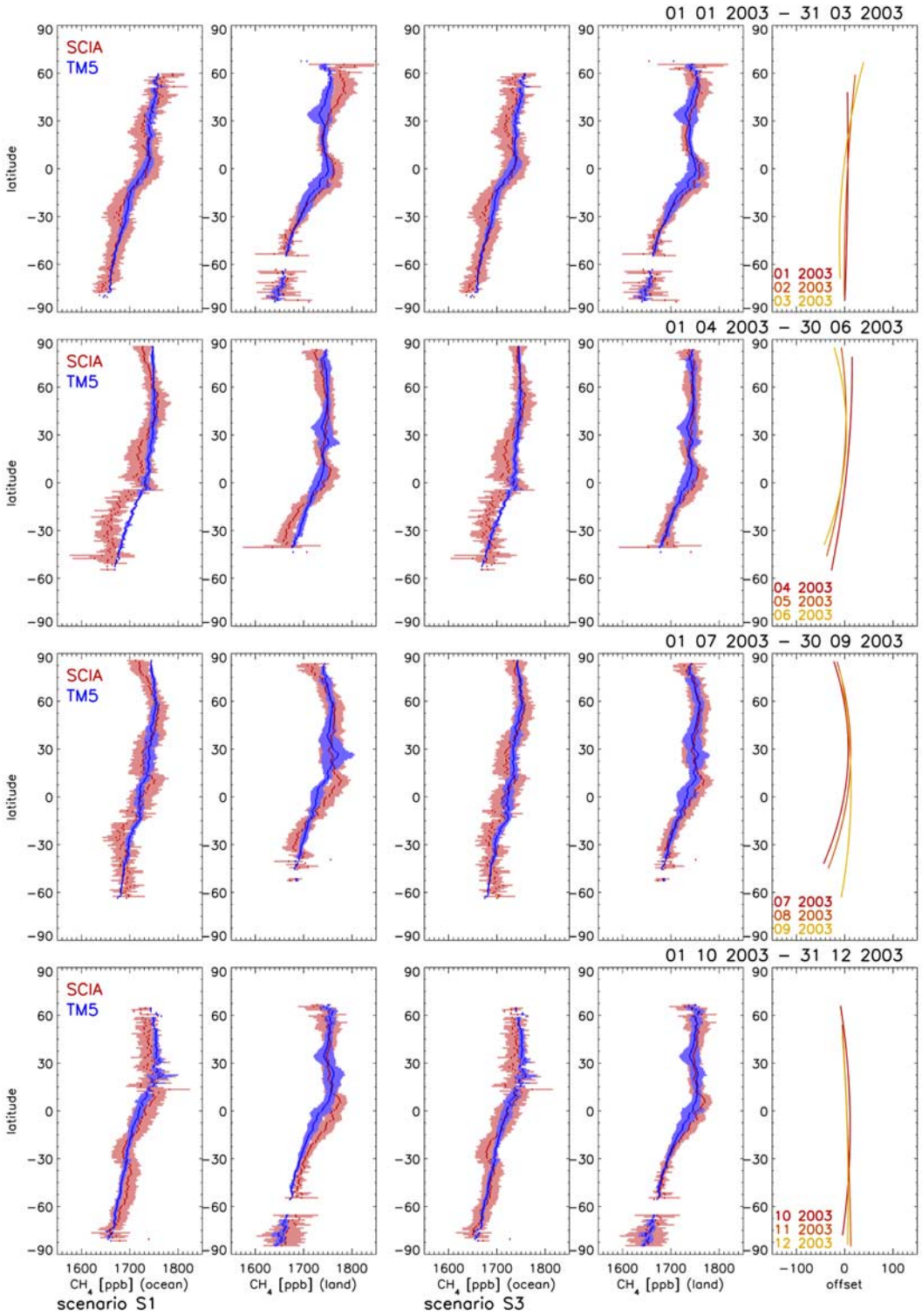

Figure 6. Comparison of latitudinal averages of SCIAMACHY measurements and TM5 simulations, shown separately for $1^\circ \times 1^\circ$ pixels over the ocean and over land. The first two columns refer to scenario S1 (first column: ocean; second column: land), the third (ocean) and fourth column (land) refer to scenario S3. The shaded areas indicate the 1σ standard deviation within the 1° latitude band (for SCIAMACHY measurements and TM5 simulations, respectively). The last column illustrates the calculated polynomials (equation (4)) used to correct bias in SCIAMACHY data as function of latitude and month, for scenario S3.

Thus, this particular feature has much higher uncertainties than the large tropical CH_4 enhancements.

[39] In the following we discuss the continental regions with the greatest CH_4 enhancements (Asia, South America, and Africa) in more detail and compare the observed spatial patterns and their seasonal evolution with TM5 $1° \times 1°$ zoom simulations over these regions (Figure 1). For a more detailed discussion of North America, Europe, and Australia the reader is referred to the auxiliary material.

4.1.2. Asia

[40] Column averaged CH_4 mixing ratios show a remarkably high spatial and temporal variability over Asia (Figure 7). During July to September, very high values are observed over India, Burma, Thailand, and large parts of southeast China, broadly consistent with the model simulations (scenario S1). According to the model, the strong signal is mainly due to emissions from rice paddies, emitting more than 28 Tg CH_4 during these 3 months. A major difference compared to the observations is higher simulated CH_4 mixing ratios in these regions during October to December, indicating that rice emissions decrease earlier than assumed in the model. We note that due to the lack of surface monitoring sites in this region, the timing was not changed significantly in scenario S1 compared to the a priori emissions. We anticipate that incorporation of SCIAMACHY data into the inversion (scenarios S3–S6) will lead to an earlier termination of rice emission in the model and hence better agreement between observations and simulation for the last quarter or the year (see section 4.2).

[41] Beside the strong seasonal signal from rice paddies, tropical wetlands also play a role, and (nearly) constant emissions from enteric fermentation and waste lead to elevated mixing ratios over southeast China throughout the year, visible both in observations and model simulations. The very low CH_4 mixing ratios over the Himalaya are mainly a topographic effect (as the total columns mainly consist of upper tropospheric and stratospheric air). However, this effect is less pronounced in the observations than in the model simulations. Indeed retrievals may have some systematic errors for large surface elevation due to large deviations of the real atmospheric state from the assumed a priori state in the retrieval algorithm. Furthermore, we note that high SCIAMACHY values in the latitude region between 40 and 50° for the 3-month composite of January to March (Figure 7) are based on very few measurements only (with relatively large scatter), therefore this is considered a relatively uncertain feature.

4.1.3. South America

[42] In South America, very high column averaged CH_4 mixing ratios are observed by SCIAMACHY over the Amazon region (Figure 8a). During January to March, model simulations agree almost perfectly with observations. According to the model simulations the strong signal over the Amazon basin is mainly due to emission from Amazon wetlands (wet season). Throughout the remainder of the year, simulated mixing ratios are decreasing, while observed values remain very high. During October to December, very high values are observed over Columbia and Venezuela, which are not reproduced by the model (although the general tendency to higher values towards the northwest is also visible in the model simulations).

[43] A very different picture emerges for scenario S2, based on the 'BW' wetland inventory (Figure 8b). For this scenario simulated CH_4 mixing ratios are much lower over the Amazon basin throughout the year. The reason for that is the very different spatial distribution of wetland emissions between the two inventories: While the 'JK' inventory attributes the major part of the emissions in the Amazon region, the 'BW' inventory attributes a large part to the Pantanal region much farther south, while assigning relatively low emissions to the Amazon basin. As mentioned above, both scenarios are compatible with the background surface measurements, and even at Christmas Island, which is most sensitive of all sites to tropical emissions from South America, relatively small differences between the model simulations for the two scenarios are found (see also auxiliary material, Figures S7 and S8). The major reason for the different spatial distribution of CH_4 emissions of the two wetland inventories seems to be the different underlying wetland distributions. While the 'JK' inventory uses the new wetland maps as described in section 3.3, the 'BW' inventory is based on the wetland distribution of *Matthews and Fung* [1987].

[44] The comparison with SCIAMACHY observations suggests that the 'JK' inventory is describing wetland emissions in South America better than the 'BW' inventory. Unfortunately, no continuous surface monitoring exists close to the wetland areas which could be used for further evaluation. Based on microwave remote sensing estimates of inundation and wetland vegetation, *Melack et al.* [2004] estimate total emissions of 29.3 Tg CH_4/yr for the whole Amazon basin below 500 m altitude, and 3.3 Tg CH_4/yr for the Pantanal. For comparison we extract the emissions of the model inventories: for the Amazon basin we use the 'rectangle' between 15°S and 5°N, and between 80°W and 45°W, excluding areas above 500 m. For the Pantanal we extract the emissions between 25°S and 15°S, and between 60°W and 55°W. In this way we derive emissions for the 'Amazon basin' of 41 Tg CH_4/yr (scenario S1; a priori: 32 Tg CH_4/yr) and 16 Tg CH_4/yr (scenario S2; a priori: 11 Tg CH_4/yr), and for the 'Pantanal' of 3.2 Tg CH_4/yr (scenario S1; a priori: 2.5 Tg CH_4/yr) and 12 Tg CH_4/yr (scenario S2; a priori: 8.8 Tg CH_4/yr). Thus, the emissions of scenario S1 are much closer to the estimate of *Melack et al.* [2004], than the emissions of S2. This is in particular true for the ratio of emissions from these two regions ('Amazon basin'/'Pantanal': *Melack et al.* [2004]: 8.9; scenario S1: 12.8; scenario S2: 1.3).

4.1.4. Africa

[45] Observed column averaged CH_4 mixing ratios show strong enhancements in Africa in the latitude belt between 10°S and 15°N (Figure 9). Model simulations of scenario S1 show lower enhancements in this latitude region, and the spatial patterns are different. While observations show a relatively uniform enhancement over most of the longitude range between 20°W and 30°E, model simulations show a more regional enhancement over the Congo basin, mainly due to wetland emissions (see far right panel of Figure 9). In addition, emissions from biomass burning are important between April and September south of the equator, and between October and March north of the equator. However, biomass burning is contributing only 1/3 of wetland emissions (10.0 Tg CH_4/yr versus 31.2 Tg CH_4/yr in

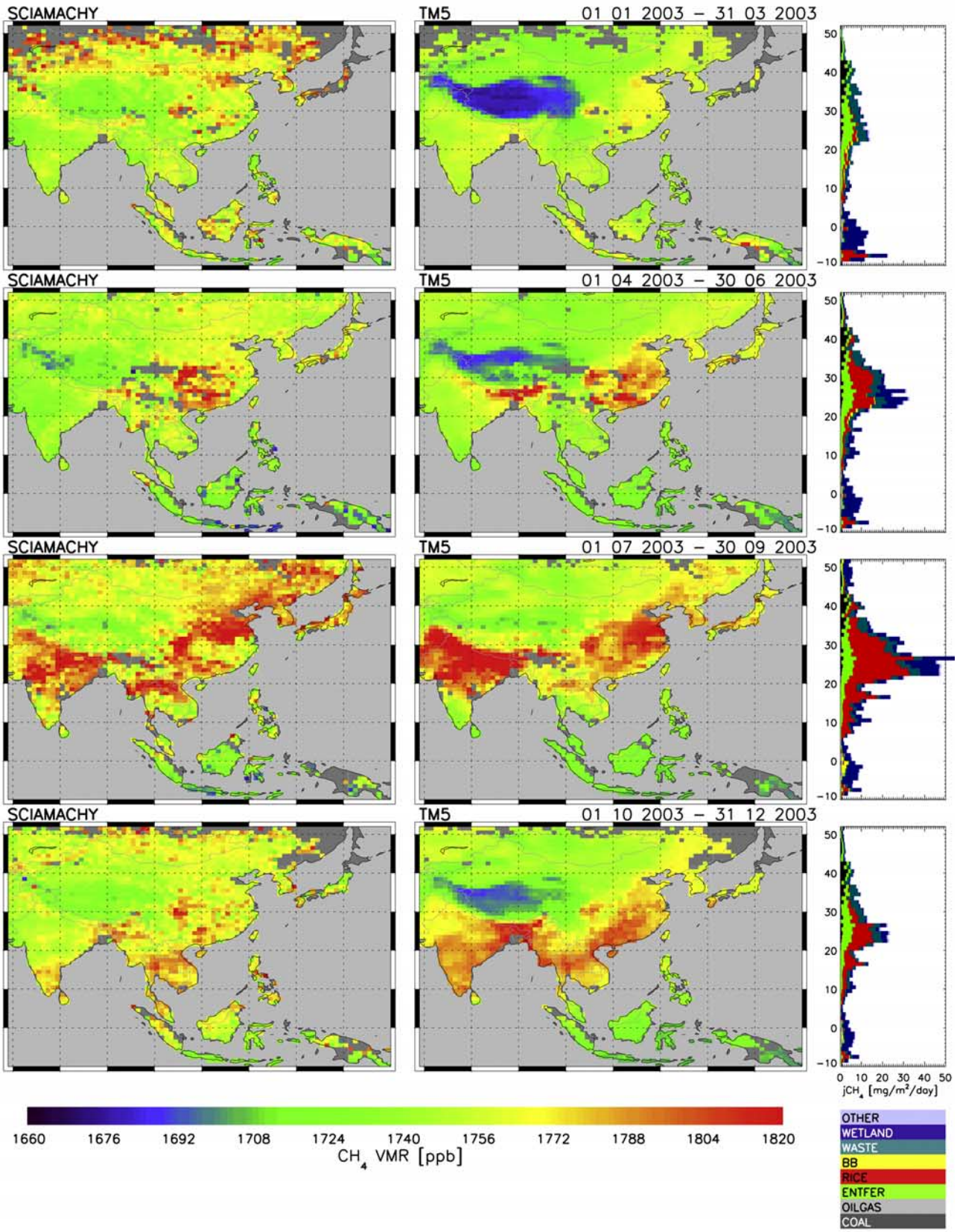

Figure 7. SCIAMACHY measurements and TM5 high-resolution (1° × 1°) simulations for Asia (scenario S1).

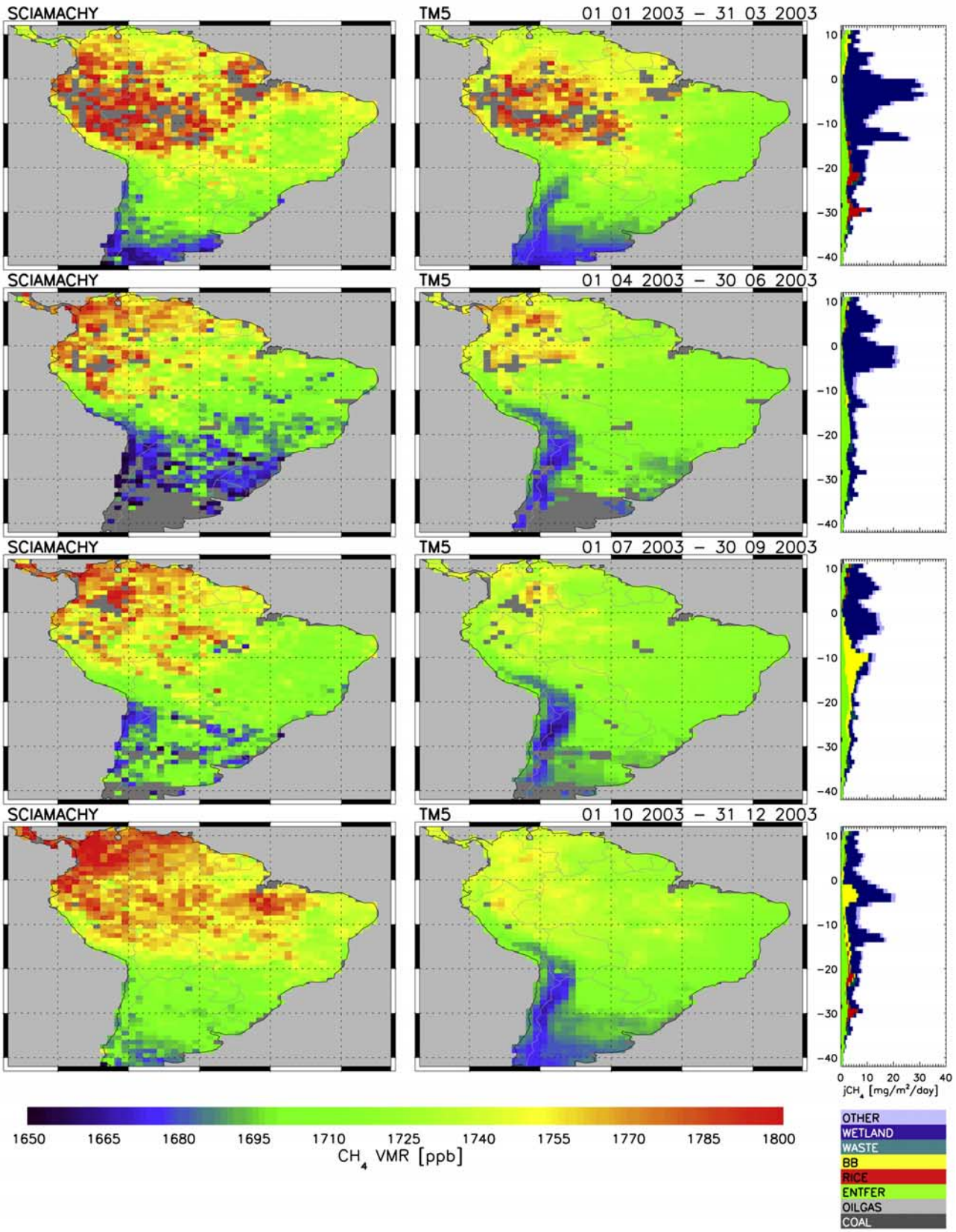

Figure 8a. SCIAMACHY measurements and TM5 high-resolution (1° × 1°) simulations for South America (scenario S1, using the 'JK' wetland inventory).

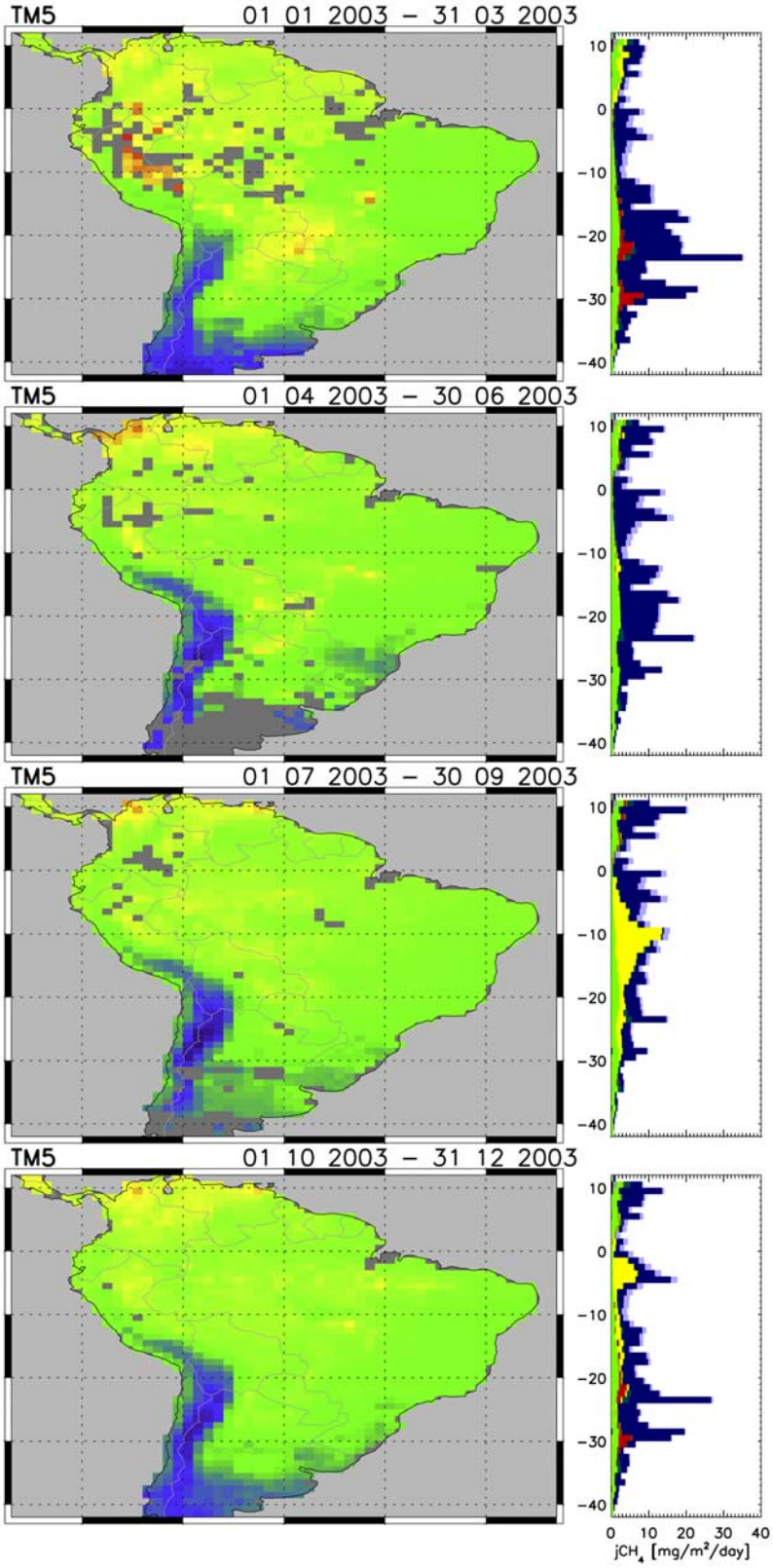

Figure 8b. TM5 high-resolution (1° × 1°) simulations for South America, scenario S2 (using the 'BW' wetland inventory). Color scale and legend are as in Figure 8a.

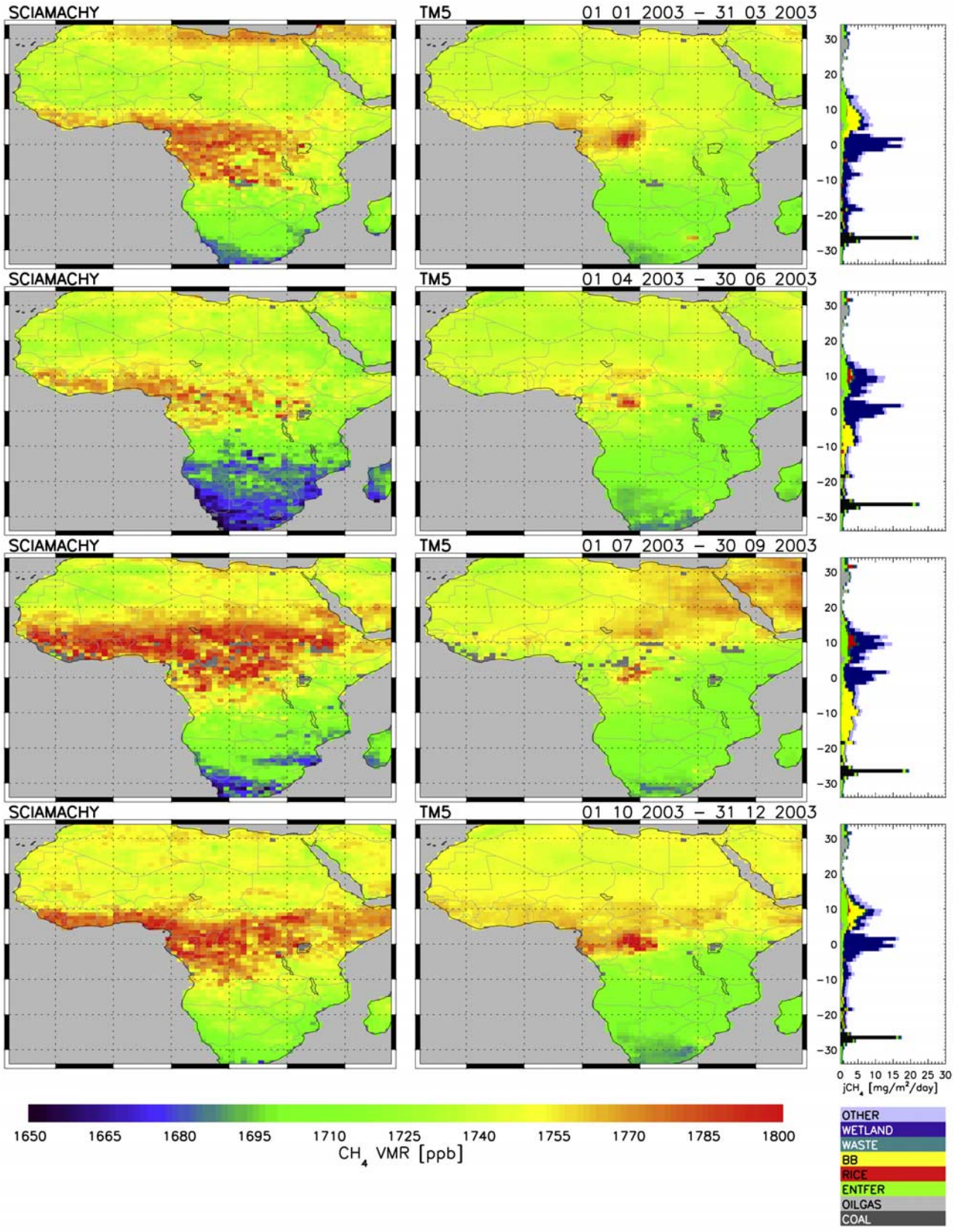

Figure 9. SCIAMACHY measurements and TM5 high-resolution (1° × 1°) simulations for Africa (scenario S1).

scenario S1), and it is much less apparent in the modeled atmospheric signal.

[46] The two wetland inventories also show significant differences for Africa: During January to June, the 'BW' inventory distributes the wetland emissions over a larger latitude region than the 'JK' inventory, resulting in poorer agreement with SCIAMACHY observations. During October to December, however, this inventory has greater emissions between 0 and 20°N, leading to better agreement with SCIAMACHY measurement than the 'JK' inventory.

[47] According to the applied IIASA/EDGAR emission inventory, CH_4 emission from coal mining in South Africa should play a significant role. In scenario S1 the total emissions from coal mining in the SH (mainly consisting of the emissions from South Africa) are scaled to 8.9 Tg CH_4/yr (a priori: 6.8 Tg CH_4/yr), leading to a clearly visible signal in the column averaged CH_4 mixing ratio in the model simulations over this region. This signal, however, is not visible in the SCIAMACHY observations (even not using a refined color scale), indicating an overestimation of these emissions in scenario S1. When including the SCIAMACHY data in the inversion (scenarios S3–S6; section 4.2) the emissions from coal mining in the SH are indeed significantly reduced (to 0.0 to 4.7 Tg CH_4/yr, see Table 3). The lower emission range is more consistent with the recent estimates of EDGAR3.2 2000 Fasttrack for South Africa amounting to 1.3 Tg CH_4/yr [*Van Aardenne et al.*, 2005].

[48] Another discrepancy between SCIAMACHY and model simulations is the very low CH_4 column averaged mixing ratios observed south of 10°S during April to June, concomitant with a similar bias during that period over Australia and over the ocean.

4.2. Inversions Based on Simultaneous Use of NOAA Surface and SCIAMACHY Measurements

[49] A key issue in the simultaneous inversion of surface and satellite observations is the compatibility of the two data sets. In section 4.1 we saw potentially significant biases between model simulations optimized with surface observations and SCIAMACHY data (i.e., scenarios S1 and S2). First test inversions using both data sets without any bias correction (and varying weighting of surface versus satellite observations) demonstrated that further optimization of the emissions is not sufficient to notably reduce the bias between SCIAMACHY and model simulations, if model results for surface observations should not deteriorate significantly (results not shown). Therefore, we have introduced a bias correction for the SCIAMACHY data, using polynomials as function of latitude and month (equation (4)). The rationale for this approach is that there is the potential for systematic errors that depend on latitude and season. Solar zenith angle (SZA) dependent air mass factors (AMFs) could be such a factor (see section 4.5). The polynomial corrections calculated in the inversion are illustrated in Figure 6 for scenario S3. This scenario is based on the simultaneous use of surface and satellite data, but it is otherwise identical to S1 (see Table 3).

[50] The derived polynomials are subtracted from the SCIAMACHY data. The global distribution of the resulting corrected SCIAMACHY data is displayed in Figure 10, together with model simulations of scenario S3.

[51] The polynomial correction results in a distinct improvement particularly for the background atmosphere of the SH, removing the seasonal bias over Australia (and other continental and oceanic regions of this latitude region) during April to June. A further effect of the polynomial correction is a significant reduction in enhanced CH_4 over northern America and Eurasia (between ~40°N and 60°N) during March.

[52] Including the SCIAMACHY observations into the inversion leads to a further increase of tropical sources (Table 3). Compared to scenario S1, scenario S3 results in larger emissions from tropical wetlands in Africa (47.1 Tg CH_4/yr compared to 31.2 Tg CH_4/yr), a further increase of CH_4 emissions from termites, and decrease of the soil sink, further enhancing net emissions from tropical regions. This is also illustrated in Figure 3. At the same time, rice paddy emissions are significantly reduced (from 52.9 ± 6.6 Tg CH_4/yr for region 'NH3' in scenario S1 to 37.9 ± 4.9 Tg CH_4/yr in scenario S3). This emission reduction is mainly from September to December, resulting in a distinct improvement in the agreement between SCIAMACHY observations and model simulations in the last quarter of the year (compare Figure 10 (scenario S3) and Figure 5 (scenario S1); see also Figure S1 of auxiliary material with high resolution simulations for scenario S3). The increase of tropical emissions in scenario S3 also leads to further improvements for tropical regions of South America and Africa. Over South America, CH_4 column averaged mixing ratios become greater over the Amazon region during the second half of the year, bringing the model simulation closer to SCIAMACHY data. However, the very high CH_4 values over Venezuela and Columbia during October to December still cannot be reproduced in scenario S3. In part, this demonstrates the limitations of the applied synthesis inversion approach with large regions, which does not allow further optimization of emission patterns within the predefined regions.

[53] Similarly, differences in the smaller scale spatial patterns over Africa and Asia remain for the model simulations of scenario S3, indicating significant deficiencies in the spatial distribution of the applied bottom-up inventories. Over Africa the observations from space suggest a spatially more homogeneous distribution of CH_4 emissions between 10°S and 15°N, while the strong enhancement over the Congo basin in the model simulations remains dominant (Figure S1d).

[54] Over Asia the main differences in the spatial fine structure are larger CH_4 mixing ratios observed over the red basin in China, northern Thailand and Burma, but smaller observed values over Bangladesh (Ganges delta), compared to model simulations (July–September) (Figure S1e). However, there are also several major emission regions (in particular during July to September, when the overall signal is largest) with very similar patterns in SCIAMACHY observations and model simulations, particularly over large parts of northern India and eastern China.

[55] In scenario S4, we apply the 'BW' wetland inventory (this scenario includes the SCIAMACHY observations, but is otherwise identical to S2). As for scenario S3 versus S1, S4 results in larger tropical emissions than S2. A striking feature is the very large emissions derived from termites (67.2 ± 6.7 Tg CH_4/yr) which seems unrealistic and is

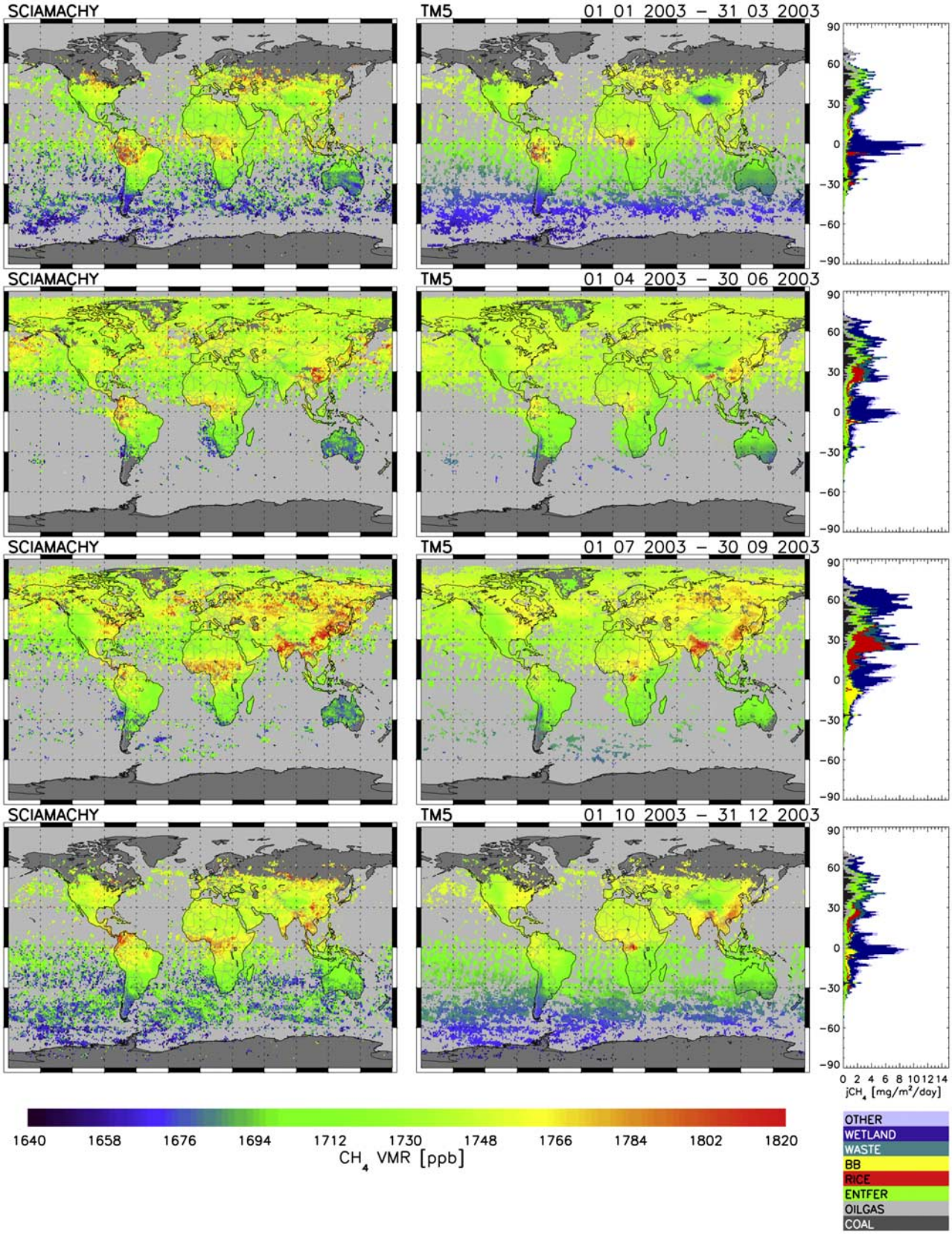

Figure 10. SCIAMACHY measurements and TM5 simulations for scenario S3. SCIAMACHY data are corrected with polynomial offset derived from the coupled inversion (equation (4)). Detailed comparison with zoom simulations is shown for all six zoom regions in the auxiliary material (Figures S1a–S1f).

probably related to compensating deficiencies in the tropical spatial distributions of the other source categories. This could also be an indication for other tropical sources not included in our base functions, such as the newly discovered CH_4 emissions from plants [*Keppler et al.*, 2006] (see section 4.4). As for scenario S2, the agreement with SCIAMACHY observations over South America remains relatively poor for scenario S4.

[56] The combined inversion leads to an only small deterioration of χ^2 for the surface data (from $\chi^2 = 1.2$ for scenarios S1 and S2 to $\chi^2 = 1.3$ for scenarios S3–S6; see Table 3). Thus the agreement of model simulations with surface observations remains very good (compare also Figure 4 (scenario S1) with Figure S9 (scenario S3)).

[57] The relatively low χ^2 of ~0.5 achieved for the SCIAMACHY data (scenarios S3–S6) indicates that the assumed uncertainty of 1.5% for monthly mean values may have been somewhat overestimated. This is also reflected in the low standard deviation between optimized model simulations and SCIAMACHY data of ~18 ppb (~1.0 %).

4.3. Sensitivity of Inverse Modeling Simulations to Global OH Sink

[58] Comparing scenarios S1 versus S2 and S3 versus S4, we investigated the sensitivity of model simulations to applied bottom-up inventories of wetland emissions, showing generally large effects over source regions but relatively small effects in the background atmosphere far from the sources. Beside CH_4 sources, the OH sink may play a significant role. As the OH sink is strongest in the tropics, the assumed OH sink will influence the derived tropical sources. We further investigate this effect in scenarios S5 and S6 for the coupled inversion (using both surface and satellite data). In these two sensitivity experiments the global OH sink is decreased by 5% (scenario S5) or increased by 5% (scenario S6). The applied OH variation of ±5% is within the typical range of interannual OH variability derived by *Dentener et al.* [2003] and *Bousquet et al.* [2005]. The compilation in Table 3 and Figure 3 illustrates that this variation in global OH affects, as expected, mainly the tropical emissions. The general conclusions drawn in section 4.2, however, are also valid for these two scenarios. Even for scenario S5 the increase in tropical emissions is larger than for scenarios S1, based on surface measurements only. Another interesting result is that the derived rice emissions from Asia (region 'NH3') are virtually identical for scenarios S3, S5, and S6. Obviously these emissions are very well constrained by the SCIAMACHY observations, and, since the large plumes (in particular during July to September) are related to very recent emissions, the effect of the OH sink is marginal. This further illustrates the added value of the SCIAMACHY observations, being sensitive to surface methane.

4.4. Relevance of Recently Discovered CH_4 Emissions From Plants

[59] The a posteriori emissions derived for scenarios S3–S6 result in significantly greater tropical emissions compared to the a priori estimate and compared to scenarios S1 and S2, confirming the conclusion drawn earlier based on forward simulations [*Frankenberg et al.*, 2006, 2005a]. The large tropical CH_4 emissions derived from the SCIAMACHY observations are attributed in the inversion to greater emissions mainly from tropical wetlands, but at the same time also an increase of CH_4 emissions from termites, and a decrease of the soil sink are calculated. Given the uncertainties in the spatial distribution of emissions and the discrepancies between simulated and observed spatial patterns, this result has to be viewed with some caution. Of particular interest in this context is the recent finding of CH_4 emissions from plants under aerobic conditions [*Keppler et al.*, 2006]. In a first attempt to upscale these measurements *Keppler et al.* [2006] estimate that global total emissions may be 149 Tg CH_4/yr (62–236 Tg CH_4/yr), with the main contribution estimated from tropical forests and grasslands (107 CH_4/yr with a range of 46–169 CH_4/yr). A significant CH_4 source from tropical forests and grasslands could indeed help to explain the rather uniform CH_4 enhancement observed by SCIAMACHY over the tropical regions of Africa and South America. This would also be consistent with the observation of a clear spatial correlation between CH_4 enhancements and occurrence of tropical rainforest [*Frankenberg et al.*, 2005a].

[60] If confirmed, this new CH_4 source would constitute a significant fraction of the total global methane emissions and have important implications for the global CH_4 budget. To accommodate it within the present budget, some sources would need to be reassessed downwards or some sinks reassessed upwards. However, we note that the approach applied by *Keppler et al.* [2006] to scale up emissions from the leaf level to global totals by using only few measured data (mainly from herbaceous species) and the Net Primary Productivity of the main biomes is very uncertain and tends to overestimate considerably the global estimates, especially for forest biomes. Furthermore, significant constraints on the upper limit of the global natural CH_4 emissions arise from the preindustrial CH_4 budget. *Houweling et al.* [2000] estimate the total preindustrial sources and sinks to be 252 (226–293) Tg CH_4/yr (year 1800). Accounting for some known small anthropogenic sources at that time (30 (15–65) Tg CH_4/yr) and some known minor natural sources (58 (38–78) Tg CH_4/yr) yields a remaining net source of 163 (130–194) Tg CH_4/yr which was entirely attributed by *Houweling et al.* [2000] to wetlands. If plant emissions contribute significantly, this would mainly imply that CH_4 emissions from wetlands have been overestimated. Assuming a lower limit for CH_4 emissions from wetlands of 90 Tg CH_4/yr would imply an upper limit of ~100 Tg CH_4/yr for the total global emissions from plants. Summarizing, we think that the additional natural CH_4 emissions from plants, located mainly in the tropics, could help in the interpretation of the SCIAMACHY observations. However, further measurements are needed, covering the major terrestrial biomes, in order to improve the upscaling of the plant emissions and to investigate their spatio-temporal emission patterns in more detail, before this new source can be realistically included in model simulations.

4.5. Potential Systematic Errors

4.5.1. Potential Systematic Errors in CH_4/CO_2 Retrievals Due to Differences in Light Path Distribution

[61] Despite the vicinity of the spectral regions used for CH_4 and CO_2 retrievals, small differences might exist in the exact light path distribution for both species due to wave-

length dependencies of surface albedo, cloud albedo, and aerosol optical properties. These effects have been discussed in detail by *Frankenberg et al.* [2006]. Summarizing, they concluded that the effect of aerosols is likely to be smaller than 1% on the retrieved CH_4/CO_2 ratio. Wavelength dependence of surface or cloud albedo, however, could introduce larger systematic errors. *Frankenberg et al.* [2006] estimated that cloud or surface albedo changes of 25% between the fitting windows of CH_4 and CO_2 may introduce a systematic error in the retrieved CH_4/CO_2 ratio of 0.5–2% for typical conditions (but could rise up to 3%).

4.5.2. Further Potential Systematic Errors in CH_4/CO_2 Retrievals

[62] Further systematic errors in the retrievals on the order of 1% or higher may arise from errors in the used spectroscopic parameters, the assumed instrumental line shape (ILS) and the assumed vertical temperature profiles [*Barkley et al.*, 2006; *Dufour and Breon*, 2003; *Frankenberg et al.*, 2005b]. *Frankenberg et al.* [2005b] showed that retrieval errors related to errors in the pressure broadening coefficients of absorption lines and related to ILS also depend on SZA.

[63] To analyze whether the observed bias between SCIAMACHY retrievals and TM5 simulations could be directly related to SZA dependence, we investigated the correlations between this bias and SZA (Figures S3a–S3c; evaluated for scenario S1). For months May to August, when this bias is largest (and correspondingly also the calculated polynomial offset in scenarios S3–S6 becomes largest; Figure 6), there is indeed a clear correlation between bias and SZA (Figure S3b), most pronounced for the data from the SH. For the remainder of the year (January–April and September–December), however, the correlation plots show more complex features, with varying correlations for subsets of the data from different latitudes, indicating a superposition of different systematic effects (including deficiencies of the modeled CH_4 distribution and CO_2 correction). The same analysis has also been performed comparing ocean pixels only (thus generally better representing background conditions), resulting in overall relatively similar correlations patterns (plots not shown).

[64] Summarizing, this first analysis indicates that part of the bias might be due to some dependence of retrieved CH_4/CO_2 on SZA, but this effect alone cannot entirely explain the bias. Furthermore, we note that effects depending more directly on latitude rather than on SZA could also show up in significant correlations with SZA (as SZA and latitude are clearly related). Clearly further research is needed to investigate these effects in more detail.

4.5.3. Potential Systematic Errors in CO_2 Correction

[65] The CO_2 correction based on the TM3 forward simulations (as described in section 2.1) leads to a significantly improved agreement between SCIAMACHY CH_4 retrievals and TM5 model simulations compared to the previous approach assuming globally constant CO_2 [*Frankenberg et al.*, 2005a]. The effect on monthly mean $\overline{VMR}(CH_4)$ values can be up to ±2.5% for certain pixels and regions (Figure S4); the effect on the longitudinal monthly average can be up to ±1.0%. Due to the significant impact of the CO_2 correction on $\overline{VMR}(CH_4)$, evaluation of the relative accuracy of applied CO_2 model fields is important. Comparison with surface measurements from the NOAA network shows overall reasonable agreement at most sites (Figure S6). However, we see also some systematic discrepancies, in particular regarding the seasonal behavior in the NH, where model simulations tend to be significantly higher (~3 ppm) than observations in late summer at several sites. *Olsen and Randerson* [2004] showed that column averaged mixing ratios may have a much smaller seasonal variation than mixing ratios at the surface (up to a factor of ~3). However, analysis of the TM3 simulations showed a much smaller difference in seasonal amplitude. For example, the simulated seasonal amplitude at Alert of about 8 ppm (Figure S6) is only slightly smaller than the mean seasonal amplitude of column averaged CO_2 at high northern latitudes (~7 ppm; Figure S5). This discrepancy to the study of *Olsen and Randerson* [2004] is probably mainly due to the too weak vertical mixing in the MATCH model [*Olsen and Randerson*, 2004], while comparison of TM3 simulations with aircraft measurements showed rather good agreement of vertical profiles [*Tiwari et al.*, 2006]. The much smaller difference in seasonal amplitude of column averaged mixing ratios compared to surface values, however, implies that the systematic error of simulated column averaged mixing ratios could be in the same order of magnitude as the discrepancies between model simulations and surface observations, i.e., up to ~1%. The use of inverse CO_2 simulations will further improve the CO_2 correction applied to the SCIAMACHY data in the future. However, inverse simulations also face the problem that they are poorly constrained by observations over large continental areas, especially in the tropics (analogous to the discussed limitations of CH_4 inverse model simulations). A further small systematic error in the present study arises from neglecting the AK of CO_2 in the calculation of column averaged CO_2 mixing ratios.

4.5.4. Potential Systematic Errors in Vertical Distribution of Model Simulations

[66] Despite the favorable agreement of inverse model simulations with surface observations (section 4.1 and Figure 4), possible systematic errors in simulated vertical distribution would result in systematic errors of column averaged mixing ratios. Critical could be especially the stratosphere, which is largely decoupled from the surface distribution. Simulated stratospheric CH_4 mixing ratios largely depend on simulated exchange between troposphere and stratosphere, simulated transport and mixing within the stratosphere, and prescribed photochemical sinks (OH, $O(^1D)$, and Cl). To evaluate the simulated CH_4 in the stratosphere above 100hPa, we used the monthly mean zonal HALOE/CLAES climatology from UARS [*Randel et al.*, 1998] (Figure S2). The major differences between TM5 simulations and the HALOE/CLAES data are the less pronounced polar vertices and slightly higher values between 100 and ~50 hPa in the model simulations. The overall impact on derived total column averaged CH_4 mixing ratios, however, is rather small. Applying the SCIAMACHY averaging kernels, and assuming a constant CH_4 mixing of 1700 ppb ratio below 100 hPa, the simulated column averaged mixing ratios are about 7 ppb higher than those derived from the HALOE/CLAES data, but vary around this offset less than 2 ppb. Only for the polar vortices the deviations from this offset are somewhat

higher (~10 ppb), but these are not relevant, since no SCIAMACHY data are retrieved for these high latitudes/seasons. The general very low impact on column averaged mixing ratios is also due to the low SCIAMACHY averaging kernels in the stratosphere (~0.3–0.6). Assuming that the HALOE/CLAES data represent the truth, we conclude that potential errors of model simulation above 100 hPa result in variations with latitude and season of simulated column averaged mixing ratio of less than 2 ppb. Hence, they are negligible for the discussed bias between SCIAMACHY and TM5.

[67] Further systematic errors of simulated total columns could arise from potential systematic errors in tropopause height in the model or from systematic errors in the middle and upper troposphere. However, observations at several high mountain sites in the free troposphere are simulated accurately, and intensive model intercomparisons and validation based on ^{222}Rn and SF_6 measurements do not hint at serious problems in the description of vertical transport processes of the TM5 model [*Bergamaschi et al.*, 2006]. Nevertheless, further validation by independent measurements, such as aircraft measurement, would be useful to exclude a significant impact of these potential errors.

5. Conclusions

5.1. Potential Systematic Errors and Validation of SCIAMACHY Retrievals

[68] SCIAMACHY provides exciting views of the global distribution of CH_4, which are very valuable for quantifying emissions from source regions which have been poorly monitored so far. However, this new CH_4 product has been poorly validated by independent observations. Identifying potential systematic errors that may change in space and time remains a key question in evaluating the quality of SCIAMACHY data. We addressed this question by using inverse model simulations to generate 3D model fields that are consistent with high-accuracy surface observations. In the background atmosphere, these model fields are relatively insensitive to different inversion scenarios, and therefore represent a robust reference. The comparison with SCIAMACHY data over remote continental and oceanic regions showed some biases (up to ~30 ppb) depending on latitude and season. The origin of this bias, however, remains unexplained.

[69] We discussed several potential systematic errors of retrievals and model simulations in section 4.5. Some of the discussed effects could be on the order of 1% or higher and hence could significantly contribute to the observed bias.

[70] A clear correlation of this bias with SZA was found for the period May–August (when the seasonal bias over Australia and other continental and oceanic regions of this latitude region is largest). For the remainder of the year, however, the correlation plots show more complex features, indicating a superposition of different systematic effects. More detailed investigation and better quantification of systematic errors is crucial to further increase confidence in CH_4 retrievals. Very critical is especially the dependence of systematic errors as function of space and time, affecting the relative accuracy of the data set.

[71] Furthermore, it is obvious that the comparison with our inverse model simulations cannot replace further validation by independent measurements. *Washenfelder et al.* [2003] and *Warneke et al.* [2005, 2006] demonstrated that high precision ground-based FTS measurements of column averaged CH_4 mixing ratios can be performed with a precision of 0.5%. So far, however, these high precision FTS measurements have been carried out only at single sites and during some ship cruises, and the number of data coincident with SCIAMACHY measurements is too small to draw conclusions regarding SCIAMACHY validation. It would be very useful to extend these high precision FTS measurements, in particular in regions, where SCIAMACHY retrievals suggest the largest discrepancies compared to model simulations with present emission inventories, e.g., in the tropical regions of South America and Africa, but also in remote continental regions as Australia. Furthermore, the combination of FTS measurements with in situ measurements, probing the entire vertical profile [*Washenfelder et al.*, 2005] appears very promising.

5.2. Validation of Bottom-Up Emission Inventories

[72] Over regions with significant CH_4 sources, column averaged CH_4 mixing ratios can be very large (~50 to 100 ppb enhancement over large scale tropical sources). Systematic errors of the retrievals which depend mainly on latitude or SZA (rather than on specific characteristics of certain regions such as surface albedo, topography, aerosol loading, clouds) have relatively little impact on the smaller-scale spatial structure of observed CH_4 enhancements. On the other hand, model simulations over sources strongly depend on the spatio-temporal distribution of applied emission inventories, which have considerable uncertainties. Therefore, global satellite observations, sensitive to surface methane, are a promising new data source for a comprehensive global validation of assumed emission inventories.

[73] Differences in the spatio-temporal distribution are apparent for emissions from wetlands. We applied a new wetland inventory ('JK'), based on new, high-resolution land cover maps, resulting in a significantly different spatial emission distribution over South America (scenario S1) compared to the wetland inventory of *Walter et al.* [2001a, 2001b] ('BW,' scenario S2). The new wetland inventory results in very good agreement between SCIAMACHY data and model simulations over the Amazon basin during the first half of the year (scenario S1), while scenario S2 leads to much lower than observed values. Furthermore, the 'JK' inventory is in much better agreement than the 'BW' inventory with remote sensing based estimates of CH_4 emissions from the Amazon basin and Pantanal by *Melack et al.* [2004]. Very high CH_4 mixing ratios observed over Venezuela and Columbia between October and December cannot be reproduced by the model simulations with either of the wetland inventories (but scenario S1 simulations are closer to observations than scenario S2 simulations). The comparison between the two scenarios clearly demonstrates that the existing surface network is not sufficient for monitoring tropical emissions. Extension of surface observations over the continents and closer to sources, particularly high-frequency measurements, would be very useful.

[74] Very large CH_4 plumes, mainly due to emissions from rice paddies, measured by SCIAMACHY between July and September over India and Southeast Asia are

largely consistent with model simulations. However, the comparison also indicates that rice emissions decrease earlier than simulated and that some differences exist in the exact spatial fine structure. Comparison of model simulations with SCIAMACHY data over Africa indicates that the applied IIASA/EDGAR inventory significantly overestimates CH_4 emissions from coal mining in South Africa.

5.3. Coupled Inversion

[75] We present the first coupled inversions (scenarios S3–S6) that simultaneously use both surface and satellite observations. We included a quadratic polynomial correction as function of latitude and month in the inversion to compensate for the potential systematic bias in the satellite observations. This polynomial correction resulted in a considerable improvement between SCIAMACHY observations and model simulations, removing the seasonal bias over Australia and other continental and oceanic regions of this latitude region between April and June. In the absence of a clear explanation for this offset, however, this polynomial correction has to be viewed with caution, and further investigation is required to resolve this issue. *Meirink et al.* [2006] demonstrated that systematic biases of satellite data may have a significant impact on derived emissions. In our study, the inverse system is further constrained by the high-accuracy surface observations, which strongly decreases the degrees of freedom of the system to follow such biases by erroneously 'optimizing' the emissions. Instead, the applied bias correction is optimized to achieve an optimal consistency between surface and satellite data. However, it is important to emphasize that our approach is only valid if systematic errors depend mainly on latitude and season. The achieved standard deviation between monthly averaged SCIAMACHY data and model simulation is about 18 ppb (~1.0 %) in scenarios S3–S6.

[76] The a posteriori emissions derived for scenarios S3–S6 result in significantly greater tropical emissions compared to the a priori estimate and compared to scenarios S1 and S2. The large tropical CH_4 emissions derived from the SCIAMACHY observations are attributed in the inversion to greater emissions mainly from tropical wetlands, but at the same time also an increase of CH_4 emissions from termites, and a decrease of the soil sink are calculated, further enhancing net emissions from tropical regions. In section 4.4 we discussed the recently discovered CH_4 emissions from plants [*Keppler et al.*, 2006]. It seems likely that this new CH_4 source contributes significantly especially to tropical CH_4 emissions. However, further measurements are required to improve the upscaling and to better characterize of spatio-temporal emission patterns of this new CH_4 source, before it can be realistically included in model simulations.

[77] The a posteriori emissions derived for rice paddies in India and Southeast Asia appear to be relatively well constrained by the SCIAMACHY data and are slightly reduced by the inversion, mainly due to an earlier termination of emissions (scenarios S3–S6).

[78] Overall the work presented in this paper demonstrates the great potential of the combined use of high-accuracy surface measurements and satellite observations, providing complementary information about the global distribution of CH_4 sources. Furthermore, it illustrates the usefulness of inverse modeling to integrate different types of observations and investigates their consistency. A major challenge, however, remains the realistic description of the uncertainties and potential biases of observations, the weighting of different data types, and the treatment of spatially and temporally varying coverage of data. In addition, more realistic descriptions of parameter covariance matrices are important (i.e., estimates of uncertainties and correlations of emissions).

[79] While the applied synthesis inversion has the advantage that it provides information on individual source categories and that it is relatively robust, advanced 4DVAR data assimilation techniques [*Elbern and Schmidt*, 2002; *Fisher and Lary*, 1995; *Meirink et al.*, 2006] will allow optimization of emissions on much smaller spatial scales and help to assign discrepancies between observed and simulated CH_4 mixing ratios to emissions from individual model grid cells.

[80] **Acknowledgments.** This work has been supported by the European Commission RTD projects EVERGREEN ("EnVisat for Environmental Regulation of GREENhouse gases," contract EVG1-CT-2002-00079, 5th Framework Programme) and GEMS ("Global and regional Earth-system (Atmosphere) Monitoring using Satellite and in-situ data," contract SIP4-CT-2004-516099, 6th Framework Programme). We thank Giacomo Grassi and Adrian Leip for detailed discussions on CH_4 emissions from plants. We are grateful to A. Segers for his assistance in preprocessing the ECMWF meteorological data as TM5 input.

References

Barkley, M. P., U. Frieß, and P. S. Monks (2006), Measuring atmospheric CO_2 from space using Full Spectral Initiation (FSI) WFM-DOAS, *Atmos. Chem. Phys. Discuss.*, *6*, 2765–2807.

Bergamaschi, P., M. Bräunlich, T. Marik, and C. A. M. Brenninkmeijer (2000), Measurements of the carbon and hydrogen isotopes of atmospheric methane at Izana, Tenerife: Seasonal cycles and synoptic-scale variations, *J. Geophys. Res.*, *105*(D11), 14,531–14,546.

Bergamaschi, P., H. Behrend, and A. Jol (Eds.) (2004), Inverse modelling of national and EU greenhouse gas emission inventories—Report of the workshop "Inverse modelling for potential verification of national and EU bottom-up GHG inventories" under the mandate of the Monitoring Mechanism Committee WG-1 23–24 October 2003, *EUR 21099 EN*, 144 pp., Sci. and Tech. Res. Ser., Eur. Comm., DG Joint Res. Cent., Inst. for Environ. and Sustainability, Ispra, Italy.

Bergamaschi, P., M. Krol, F. Dentener, A. Vermeulen, F. Meinhardt, R. Graul, M. Ramonet, W. Peters, and E. J. Dlugokencky (2005), Inverse modelling of national and European CH_4 emissions using the atmospheric zoom model TM5, *Atmos. Chem. Phys.*, *5*, 2431–2460.

Bergamaschi, P., et al. (2006), Model inter-comparison on transport and chemistry—Report on model inter-comparison performed within European Commission FP5 project EVERGREEN ("Global satellite observation of greenhouse gas emissions"), *EUR 22241 EN*, 53 pp., Sci. and Tech. Res. Ser., Eur. Comm., DG Joint Res. Cent., Inst. for Environ. and Sustainability, Ispra, Italy.

Bousquet, P., D. A. Hauglustaine, P. Peylin, C. Carouge, and P. Ciais (2005), Two decades of OH variability as inferred by an inversion of atmospheric transport and chemistry of methyl chloroform, *Atmos. Chem. Phys.*, *5*, 2635–2656.

Brühl, C., and P. J. Crutzen (1993), The MPIC 2D model, *NASA Ref. Publ.*, *1292*, 103–104.

Buchwitz, M., et al. (2005a), Atmospheric methane and carbon dioxide from SCIAMACHY satellite data: Initial comparison with global models of chemistry and transport, *Atmos. Chem. Phys.*, *5*, 941–962.

Buchwitz, M., R. de Beek, S. Noel, J. P. Burrows, H. Bovensmann, H. Bremer, P. Bergamaschi, S. Körner, and M. Heimann (2005b), Carbon monoxide, methane and carbon dioxide columns retrieved from SCIAMACHY by WFM-DOAS: Year 2003 initial data set, *Atmos. Chem. Phys.*, *5*, 3313–3329.

Chen, Y.-H., and R. G. Prinn (2006), Estimation of atmospheric methane emissions between 1996 and 2001 using a three-dimensional global chemical transport model, *J. Geophys. Res.*, *111*, D10307, doi:10.1029/2005JD006058.

Christensen, T. R., I. C. Prentice, J. Kaplan, A. Haxeltine, and S. Sitch (1996), Methane flux from northern wetlands and tundra: An ecosystem source modelling approach, *Tellus, Ser. B*, *48*, 652–661.

Clerbaux, C., J. Hadji-Lazaro, S. Turquety, G. Mégie, and P.-F. Coheur (2003), Trace gas measurements from infrared satellite for chemistry and climate applications, *Atmos. Chem. Phys.*, *3*, 1495–1508.

Crevoisier, C., A. Chedin, and N. A. Scott (2003), AIRS channel selection for CO_2 and other trace-gas retrievals, *Q. J. R. Meteorol. Soc.*, *129*(593), 2719–2740.

Dentener, F., W. Peters, M. Krol, M. van Weele, P. Bergamaschi, and J. Lelieveld (2003), Inter-annual-variability and trend of CH_4 lifetime as a measure for OH changes in the 1979–1993 time period, *J. Geophys. Res.*, *108*(D15), 4442, doi:10.1029/2002JD002916.

Dentener, F., D. Stevenson, J. Cofala, R. Mechler, M. Amann, P. Bergamaschi, F. Raes, and R. Derwent (2005), The impact of air pollutant and methane emission controls on tropospheric ozone and radiative forcing: CTM calculations for the period 1990–2030, *Atmos. Chem. Phys.*, *5*, 1731–1755.

Dils, B., et al. (2006), Comparisons between SCIAMACHY and ground-based FTIR data for total columns of CO, CH_4, CO_2 and N_2O, *Atmos. Chem. Phys.*, *6*, 1953–1976.

Dlugokencky, E. J., L. P. Steele, P. M. Lang, and K. A. Masarie (1994), The growth rate and distribution of atmospheric methane, *J. Geophys. Res.*, *99*, 17,021–17,043.

Dlugokencky, E. J., S. Houweling, L. Bruhwiler, K. A. Masarie, P. M. Lang, J. B. Miller, and P. P. Tans (2003), Atmospheric methane levels off: Temporary pause or a new steady state?, *Geophys. Res. Lett.*, *30*(19), 1992, doi:10.1029/2003GL018126.

Dlugokencky, E. J., R. C. Myers, P. M. Lang, K. A. Masarie, A. M. Crotwell, K. W. Thoning, B. D. Hall, J. W. Elkins, and L. P. Steele (2005), Conversion of NOAA atmospheric dry air CH_4 mole fractions to a gravimetrically prepared standard scale, *J. Geophys. Res.*, *110*, D18306, doi:10.1029/2005JD006035.

Dufour, E., and F. Breon (2003), Spaceborne estimate of atmospheric CO_2 column by use of the differential absorption method: Error analysis, *Appl. Opt.*, *42*, 3595–3609.

Elbern, H., and H. Schmidt (2002), Chemical 4D variational data assimilation and its numerical implications for case study analyses, in *Atmospheric Modeling, IMA Volumes in Mathematics and Its Applications*, edited by D. P. Chock and G. R. Carmichael, pp. 165–184, Springer, New York.

Etheridge, D. M., G. I. Pearman, and P. J. Fraser (1992), Changes in tropospheric methane between 1841 and 1978 from a high accumulation-rate Antarctic ice core, *Tellus, Ser. B*, *44*, 282–294.

European Centre for Medium-Range Weather Forecasts (ECMWF) (2002), IFS documentation, Reading, UK. (Available at http://www.ecmwf.int/research/ifsdocs/)

European Topic Centre on Terrestrial Environment (ETCTE) (2000), Corine land cover database (Version 12/2000 extended coverage), Eur. Environ. Agency, Copenhagen. (Available at http://dataservice.eea.eu.int/dataservice/metadetails.asp?id=571)

Fisher, M., and D. J. Lary (1995), Lagrangian four-dimensional variational data assimilation of chemical species, *Q. J. R. Meteorol. Soc.*, *121*, 1681–1704.

Frankenberg, C., J. F. Meirink, M. van Weele, U. Platt, and T. Wagner (2005a), Assessing methane emissions from global space-borne observations, *Science*, *308*, 1010–1014.

Frankenberg, C., U. Platt, and T. Wagner (2005b), Iterative maximum a posteriori (IMAP)-DOAS for retrieval of strongly absorbing trace gases: Model studies for CH_4 and CO_2 retrieval from near infrared spectra of SCIAMACHY onboard ENVISAT, *Atmos. Chem. Phys.*, *5*, 9–22.

Frankenberg, C., J. F. Meirink, P. Bergamaschi, A. P. H. Goede, M. Heimann, S. Körner, U. Platt, M. van Weele, and T. Wagner (2006), Satellite chartography of atmospheric methane from SCIAMACHY on board ENVISAT: Analysis of the years 2003 and 2004, *J. Geophys. Res.*, *111*, D07303, doi:10.1029/2005JD006235.

Fung, I., J. John, J. Lerner, E. Matthews, M. Prather, L. P. Steele, and P. J. Fraser (1991), Three-dimensional model synthesis of the global methane cycle, *J. Geophys. Res.*, *96*, 13,033–13,065.

Gurney, K. R., et al. (2002), Towards robust regional estimates of CO_2 sources and sinks using atmospheric transport models, *Nature*, *415*, 626–630.

Heimann, M., and S. Koerner (2003), The Global Atmospheric Tracer Model TM3: Model description and users manual release 3.8a, no.5, Max Planck Inst. for Biogeochem. (MPI-BGC), Jena, Germany.

Hein, R., P. J. Crutzen, and M. Heimann (1997), An inverse modeling approach to investigate the global atmospheric methane cycle, *Global Biogeochem. Cycles*, *11*, 43–76.

Hirsch, A. I., A. M. Michalak, L. M. Bruhwiler, W. Peters, E. J. Dlugokencky, and P. P. Tans (2006), Inverse modeling estimates of the global nitrous oxide surface flux from 1998–2001, *Global Biogeochem. Cycles*, *20*, GB1008, doi:10.1029/2004GB002443.

Houweling, S., F. Dentener, and J. Lelieveld (1998), The impact of nonmethane hydrocarbon compounds on tropospheric photochemistry, *J. Geophys. Res.*, *103*(D9), 10,673–10,696.

Houweling, S., T. Kaminski, F. Dentener, J. Lelieveld, and M. Heimann (1999), Inverse modeling of methane sources and sinks using the adjoint of a global transport model, *J. Geophys. Res.*, *104*(D21), 26,137–26,160.

Houweling, S., F. J. Dentener, and J. Lelieveld (2000), Simulation of pre-industrial atmospheric methane to constrain the global source strength of natural wetlands, *J. Geophys. Res.*, *105*, 17,243–17,255.

Intergovernmental Panel on Climate Change (IPCC) (2000), *Good Practice Guidance and Uncertainty Management in National Greenhouse Gas Inventories*, edited by J. Penman et al., Inst. for Global Environ. Strategies, Kanagawa, Japan.

Intergovernmental Panel on Climate Change (IPCC) (2001), *Climate Change 2001: The Scientific Basis. Contribution of Working Group I to the Third Assessment Report of the International Panel on Climate Change*, edited by J. T. Houghton et al., 881 pp., Cambridge Univ. Press, New York.

Joint Research Centre (JRC) (2003), Global Land Cover 2000 database, Eur. Comm., Ispra, Italy. (Available at http://www.gvm.jrc.it/glc2000)

Kaminski, T., P. J. Rayner, M. Heimann, and I. G. Enting (2001), On aggregation errors in atmospheric transport inversions, *J. Geophys. Res.*, *106*(D5), 4703–4715.

Kaplan, J. O. (2002), Wetlands at the Last Glacial Maximum: Distribution and methane emissions, *Geophys. Res. Lett.*, *29*(6), 1079, doi:10.1029/2001GL013366.

Keppler, F., J. T. G. Hamilton, M. Braß, and T. Röckmann (2006), Methane emissions from terrestrial plants under aerobic conditions, *Nature*, *439*, 187–191.

Klaassen, G., M. Amann, C. Berglund, J. Cofala, L. Hoeglund-Isaksson, C. Heyes, R. Mechler, A. Tohka, W. Schoepp, and W. Winiwarter (2004), The extension of the RAINS model to greenhouse gases, *IIASA Interim Rep. IR-04-015*, 134 pp., Int. Inst. for Appl. Syst. Anal., Laxenburg.

Krol, M. C., S. Houweling, B. Bregman, M. van den Broek, A. Segers, P. van Velthoven, W. Peters, F. Dentener, and P. Bergamaschi (2005), The two-way nested global chemistry-transport zoom model TM5: Algorithm and applications, *Atmos. Chem. Phys.*, *5*, 417–432.

Lehner, B., and P. Döll (2001), WELAREM1: A global wetlands, lakes and reservoirs data set, Univ. of Kassel, Kassel, Germany. (Available at http://www.usf.uni-kassel.de/usf/archiv/daten/lake.en.htm)

Lelieveld, J., P. J. Crutzen, and F. J. Dentener (1998), Changing concentration, lifetime and climate forcing of atmospheric methane, *Tellus, Ser. B*, *50*, 128–150.

Matthews, E., and I. Fung (1987), Methane emissions from natural wetlands: Global distribution, area, and environmental characteristics of sources, *Global Biogeochem. Cycles*, *1*, 61–86.

Matthews, E., I. Fung, and J. Lerner (1991), Methane emission from rice cultivation: Geographic and seasonal distribution of cultivated areas and emissions, *Global Biogeochem. Cycles*, *5*, 3–24.

Meirink, J. F., H. J. Eskes, and A. P. H. Goede (2006), Sensitivity analysis of methane emissions derived from SCIAMACHY observations through inverse modelling, *Atmos. Chem. Phys.*, *6*, 1275–1292.

Melack, J. M., L. L. Hess, M. Gastil, B. R. Forsberg, S. K. Hamilton, I. B. T. Lima, and E. M. L. M. Novo (2004), Regionalization of methane emissions in the Amazon Basin with microwave remote sensing, *Global Change Biol.*, *10*, 1–15, doi:10.1111/j.1529-8817.2003.00763.x.

Mikaloff Fletcher, S. E., P. P. Tans, L. M. Bruhwiler, J. B. Miller, and M. Heimann (2004a), CH_4 sources estimated from atmospheric observations of CH_4 and its $^{13}C/^{12}C$ isotopic ratios: 1. Inverse modeling of source processes, *Global Biogeochem. Cycles*, *18*, GB4004, doi:10.1029/2004GB002223.

Mikaloff Fletcher, S. E., P. P. Tans, L. M. Bruhwiler, J. B. Miller, and M. Heimann (2004b), CH_4 sources estimated from atmospheric observations of CH_4 and its $^{13}C/^{12}C$ isotopic ratios: 2. Inverse modeling of CH_4 fluxes from geographical regions, *Global Biogeochem. Cycles*, *18*, GB4005, doi:10.1029/2004GB002224.

Mitchell, T. D., and P. D. Jones (2005), An improved method of constructing a database of monthly climate observations and associated high-resolution grids, *Int. J. Climatol.*, *25*(6), 693–712.

New, M., D. Lister, M. Hulme, and I. Makin (2002), A high-resolution data set of surface climate over global land areas, *Clim. Res.*, *21*, 1–25.

Olivier, J. G. J., and J. J. M. Berdowski (2001), Global emissions sources and sinks, in *The Climate System*, edited by J. J. M. Berdowski, R. Guicherit, and B. J. Heij, A. A. Balkema, Brookfield, Vt.

Olsen, S. C., and J. T. Randerson (2004), Differences between surface and column atmospheric CO_2 and implications for carbon cycle research, *J. Geophys. Res.*, *109*, D02301, doi:10.1029/2003JD003968.

Peters, W., M. C. Krol, L. Bruhwiler, E. J. Dlugokencky, G. Dutton, J. B. Miller, P. Bergamaschi, F. J. Dentener, P. van Velthoven, and P. P. Tans (2004), Towards regional scale inversion using a two-way nested global model: Characterization of transport using SF_6, *J. Geophys. Res.*, *109*, D19314, doi:10.1029/2004JD005020.

Petit, J., et al. (1999), Climate and atmospheric history of the past 420,000 years from the Vostok ice core, Antarctica, *Nature*, *399*(6735), 429–436.

Prinn, R., D. Cunnold, R. Rasmussen, P. Simmonds, F. Alyea, A. Crawford, P. Fraser, and R. Rosen (1990), Atmospheric emissions and trends of nitrous oxide deduced from 10 years of ALE-GAGE data, *J. Geophys. Res.*, *95*(D11), 18,369–18,385.

Randel, W. J., F. Wu, J. M. Russel III, A. Roche, and J. W. Waters (1998), Seasonal cycles and QBO variations in stratospheric CH_4 and H_2O observed in UARS HALOE data, *J. Atmos. Sci.*, *55*, 163–185.

Ridgwell, A. J., S. J. Marshall, and K. Gregson (1999), Consumption of atmospheric methane by soils: A process-based model, *Global Biogeochem. Cycles*, *13*(1), 59–70.

Rödenbeck, C., S. Houweling, M. Gloor, and M. Heimann (2003), CO_2 flux history 1982–2001 inferred from atmospheric data using a global inversion of atmospheric transport, *Atmos. Chem. Phys.*, *3*, 1919–1964.

Sanderson, M. G. (1996), Biomass of termites and their emissions of methane and carbon dioxide: A global database, *Global Biogeochem. Cycles*, *10*, 543–557.

Shindell, D. T., B. P. Walter, and G. Faluvegi (2004), Impacts of climate change on methane emissions from wetlands, *Geophys. Res. Lett.*, *31*, L21202, doi:10.1029/2004GL021009.

Sitch, S., et al. (2003), Evaluation of ecosystem dynamics, plant geography and terrestrial carbon cycling in the LPJ dynamic global vegetation model, *Global Change Biol.*, *9*, 161–185.

Spahni, R., et al. (2005), Atmospheric methane and nitrous oxide of the late Pleistocene from Antarctic ice cores, *Science*, *310*, 1317–1321.

Tarnocai, C., I. M. Kettles, and B. Lacelle (2000), Peatlands of Canada Database, *Open File Rep. 3834*, Geol. Surv. of Can., Ottawa, Ont., Canada.

Tiwari, Y. K., M. Gloor, R. J. Engelen, F. Chevallier, C. Rödenbeck, S. Körner, P. Peylin, B. H. Braswell, and M. Heimann (2006), Comparing CO_2 retrieved from Atmospheric Infrared Sounder with model predictions: Implications for constraining surface fluxes and lower-to-upper troposphere transport, *J. Geophys. Res.*, *111*, D17106, doi:10.1029/2005JD006681.

Turquety, S., J. Hadji-Lazaro, C. Clerbaux, D. A. Hauglustaine, S. A. Clough, V. Casse, P. Schlüssel, and G. Megie (2004), Operational trace gas retrieval algorithm for the Infrared Atmospheric Sounding Interferometer, *J. Geophys. Res.*, *109*, D21301, doi:10.1029/2004JD004821.

Van Aardenne, J. A., F. J. Dentener, J. G. J. Olivier, J. A. H. W. Peters, and L. N. Ganzeveld (2005), The EDGAR 3.2 Fast Track 2000 dataset (32FT2000), Neth. Environ. Assess. Agency, Bilthoven, Netherlands. (Available at http://www.mnp.nl/edgar/model/v32ft2000edgar/docv32ft2000/index.jsp)

van der Werf, G. R., J. T. Randerson, G. J. Collatz, L. Giglio, P. S. Kasibhatla, A. F. Arellano Jr., S. C. Olsen, and E. S. Kasischke (2004), Continental-scale partitioning of fire emissions during the 1997 to 2001 El Nino/LaNina period, *Science*, *303*, 73–76.

Vogelmann, J. E., S. M. Howard, L. Yang, C. R. Larson, B. K. Wylie, and N. Van Driel (2001), Completion of the 1990s national land cover data set for the conterminous United States from Landsat thematic mapper data and ancillary data sources, *Photogramm. Eng. Remote Sens.*, *67*, 650–652.

Walter, B. P., and M. Heimann (2000), A process-based, climate-sensitive model to derive methane emissions from natural wetlands: Application to five wetland sites, sensitivity to model parameters, and climate, *Global Biogeochem. Cycles*, *14*(3), 745–765.

Walter, B. P., M. Heimann, and E. Matthews (2001a), Modeling modern methane emissions from natural wetlands: 1. Model description and results, *J. Geophys. Res.*, *106*, 34,189–34,206.

Walter, B. P., M. Heimann, and E. Matthews (2001b), Modeling modern methane emissions from natural wetlands: 2. Interannual variations 1982–1993, *J. Geophys. Res.*, *106*, 34,207–34,217.

Warneke, T., R. de Beek, M. Buchwitz, J. Notholt, A. Schulz, V. Velazco, and O. Schrems (2005), Shipborne solar absorption measurements of CO_2, CH_4, N_2O and CO and comparison with SCIAMACHY WFM-DOAS retrievals, *Atmos. Chem. Phys.*, *5*, 2029–2034.

Warneke, T., J. F. Meirink, P. Bergamaschi, J.-U. Grooß, J. Notholt, G. C. Toon, V. Velazco, A. P. H. Goede, and O. Schrems (2006), Seasonal and latitudinal variation of atmospheric methane: A ground-based and shipborne solar IR spectroscopic study, *Geophys. Res. Lett.*, *33*, L14812, doi:10.1029/2006GL025874.

Washenfelder, R. A., P. O. Wennberg, and G. C. Toon (2003), Tropospheric methane retrieved from ground-based near-IR solar absorption spectra, *Geophys. Res. Lett.*, *30*(23), 2226, doi:10.1029/2003GL017969.

Washenfelder, R. A., V. Sherlok, B. J. Connor, G. C. Toon, and P. O. Wennberg (2005), Initial results from the total carbon column observing network, paper presented at Seventh International Carbon Dioxide Conference, Boulder, Colo., 25–30 Sept. (Oral presentation and extended abstract available from https://www.icdc7.com/article43.html)

P. Bergamaschi, F. Dentener, and J. O. Kaplan, European Commission - DG Joint Research Centre, Institute for Environment and Sustainability, I-21020 Ispra (Va), Italy. (peter.bergamaschi@jrc.it)

E. J. Dlugokencky, Global Monitoring Division, Earth System Research Laboratory, NOAA, Boulder, CO 80305, USA.

C. Frankenberg, U. Platt, and T. Wagner, Institute of Environmental Physics, University of Heidelberg, D-69120 Heidelberg, Germany.

A. Goede, Royal Netherlands Meteorological Institute, NL-3730 De Bilt, Netherlands.

M. Heimann and S. Körner, Max Planck Institute for Biogeochemistry, D-07701 Jena, Germany.

M. Krol, Netherlands Institute for Space Research, NL-3584 Utrecht, Netherlands.

J. F. Meirink, Institute for Marine and Atmospheric Research Utrecht, University of Utrecht, NL-3584 Utrecht, Netherlands.